Temporal and spatial variability in the hydrothermal signature of sinking particles and sediments in the Western Tropical South Pacific Ocean

Chloé Tilliette[1], Frédéric Gazeau[1], Valerie Chavagnac[2], Nathalie Leblond[3], Maryline Montanes[1], Karine Leblanc[4], Sabine Schmidt[5], Bruno Charrière[6], Nagib Bhairy[4], and Cécile Guieu[7]

[1]Sorbonne Université, CNRS, Laboratoire d'Océanographie de Villefranche
[2]Geosciences Environnement Toulouse, Université de Toulouse
[3]LOV-CNRS UMR 7093
[4]MIO, CNRS - Université Aix-Marseille
[5]Université de Bordeaux, EPOC, UMR 5805 CNRS
[6]CEFREM
[7]Laboratoire d'Océanographie de Villefranche, LOV

March 16, 2023

Abstract

Iron (Fe) is an essential micronutrient for phytoplankton, particularly diazotrophs, which are abundant in the Western Tropical South Pacific Ocean (WTSP). Their success depends on the numerous trace metals, particularly iron, released from shallow hydrothermal vents along the Tonga Arc. This study aimed to explore the impact of hydrothermal fluids on particulate trace metal concentrations and biological activity. To identify the composition of sinking particles across a wide area of the WTSP, we deployed sediment traps at various depths, both close and further west of the Tonga Arc. Seafloor sediments were cored at these deployment sites, including at a remote location in the South Pacific Gyre. The sinking particles were composed of a large amount of biological material, indicative of the high productivity of the Lau Basin. A significant portion of this material was lithogenic of hydrothermal origin, as revealed through Al-Fe-Mn tracing. The sinking material showed similar patterns between lithogenic and biogenic fractions, indicating that hydrothermal input within the photic layer triggered surface production. A hydrothermal fingerprint was suggested in the sediments due to the high sedimentation rates and the presence of large, heterogeneous, trace metal-rich particles. The presence of nearby active deep hydrothermal sources was suspected near the Lau Ridge due to the large particle size and the significant enrichment of Fe and Mn. Overall, this study revealed that deep and shallow hydrothermal sources along with submarine volcanism have a significant influence on the biogeochemical signature of particles in the Lau Basin at large spatial and temporal scales.

Hosted file

`958490_0_art_file_10793493_rrgqqk.docx` available at https://authorea.com/users/514732/articles/629777-temporal-and-spatial-variability-in-the-hydrothermal-signature-of-sinking-particles-and-sediments-in-the-western-tropical-south-pacific-ocean

Temporal and spatial variability in the hydrothermal signature of sinking particles and sediments in the Western Tropical South Pacific Ocean

Chloé Tilliette[1], Frédéric Gazeau[1], Valérie Chavagnac[2], Nathalie Leblond[1], Maryline Montanes[1], Karine Leblanc[3], Sabine Schmidt[4], Bruno Charrière[5], Nagib Bhairy[3], Cécile Guieu[1*]

[1]Sorbonne Université, CNRS, Laboratoire d'Océanographie de Villefranche, LOV, 06230, Villefranche-sur-Mer, France

[2]Géosciences Environnement Toulouse, GET, CNRS, UPS, Université de Toulouse, IRD, Toulouse, France

[3]Aix Marseille Univ., Université de Toulon, CNRS, IRD, MIO, Marseille, France.

[4]Univ. Bordeaux, CNRS, Bordeaux INP, EPOC, UMR 5805, F-33600 Pessac, France

[5]Centre de Formation et de Recherche sur l'Environnement Méditerranéen (CEFREM, UMR CNRS 5110), Bât. U, Université de Perpignan, Via Domitia (UPVD), Perpignan, France

*** Correspondence:**
Chloé Tilliette, Cécile Guieu
chloe.tilliette@imev-mer.fr; cecile.guieu@imev-mer.fr

Keywords: hydrothermal sources, biological production, composition of sinking and sedimented material, metals, Tonga volcanic Arc, Western Tropical South Pacific Ocean

Number of words: 8,138

Number of tables/figures: 3 tables, 7 figures

Abstract

Iron (Fe) is an essential micronutrient for phytoplankton, particularly diazotrophs, which are abundant in the Western Tropical South Pacific Ocean (WTSP). Their success depends on the numerous trace metals, particularly iron, released from shallow hydrothermal vents along the Tonga Arc. This study aimed to explore the impact of hydrothermal fluids on particulate trace metal concentrations and biological activity. To identify the composition of sinking particles across a wide area of the WTSP, we deployed sediment traps at various depths, both close and further west of the Tonga Arc. Seafloor sediments were cored at these deployment sites, including at a remote location in the South Pacific Gyre. The sinking particles were composed of a large amount of biological material, indicative of the

high productivity of the Lau Basin. A significant portion of this material was lithogenic of hydrothermal origin, as revealed through Al-Fe-Mn tracing. The sinking material showed similar patterns between lithogenic and biogenic fractions, indicating that hydrothermal input within the photic layer triggered surface production. A hydrothermal fingerprint was suggested in the sediments due to the high sedimentation rates and the presence of large, heterogeneous, trace metal-rich particles. The presence of nearby active deep hydrothermal sources was suspected near the Lau Ridge due to the large particle size and the significant enrichment of Fe and Mn. Overall, this study revealed that deep and shallow hydrothermal sources along with submarine volcanism have a significant influence on the biogeochemical signature of particles in the Lau Basin at large spatial and temporal scales.

Plain Language Summary

Iron is an essential micronutrient for phytoplankton growth, especially diazotrophs. In a certain area of the Pacific Ocean, they can obtain the iron they need from material released by hydrothermal vents along the Tonga Arc. The aim of this study was to understand how hydrothermal sources affect the amount of iron and other materials released into the water column and their influence on phytoplankton. We collected sinking particles and seafloor sediments and examined their chemical composition. The sinking material consisted of a large amount of biological material, indicative of the high productivity of the area. A large part of the particles collected were minerals from hydrothermal vents. These biological and metallic materials displayed similar export patterns, indicating the role of hydrothermal sources in driving surface ocean productivity. Seafloor sediments were also influenced by hydrothermalism, as suggested by their high metal contents, high sedimentation rates and large, heterogeneous particle size. In addition, an undiscovered hydrothermal source was potentially identified near the Lau Ridge based on these data. Overall, this study revealed the significant impact of hydrothermalism on the biogeochemical signature of the particules in the Lau Basin at large spatial and temporal scales.

1 Introduction

The Western Tropical South Pacific (WTSP) Ocean (160 °E to 160 °W) has been identified as a hotspot for dinitrogen (N_2) fixation by diazotroph organisms (Bonnet et al., 2017). The success of these species relies on the high, non-limiting surface concentrations of iron (Fe) in the region, as Fe is a major component of the nitrogenase enzyme that catalyzes the N_2 fixation process (Raven, 1988). Recently, Tilliette et al. (2022) revealed that these high dissolved Fe (DFe) concentrations originate from shallow hydrothermal sources (< 300 m) hosted along the Tonga-Kermadec Arc that fertilize the photic zone of the entire Lau Basin with DFe, forming a productivity patch as large as 360,000 km² (analogous to the Caspian Sea area; Bonnet et al., in rev.).

The Tonga-Kermadec Arc is the most linear, convergent and seismically active subduction zone on Earth (Timm et al., 2013) and consequently exhibits the highest density of submarine volcanoes and associated hydrothermal sources (Massoth et al., 2007; Pelletier et al., 1998; Stoffers et al., 2006). Such systems release extensive plumes enriched in numerous chemical species relative to the overlying water column (Dick et al., 2013; González-Vega et al., 2020; Lilley et al., 2013) including gases (e.g., H_2S – hydrogen sulfide, CO_2 – carbon dioxide, CH_4 – methane), macronutrients and dissolved and particulate trace metals (e.g., Fe, Mn – manganese, Cu – copper, Zn – zinc, Pb – lead, Ni – nickel). In the Lau Basin, most of these plumes originate from sources located at depth (> 1000 m; Beaulieu and Szafrański, 2020; Lupton et al., 2004; Massoth et al., 2007), but shallower active sources (< 500 m) have also been identified (Beaulieu and Szafrański, 2020; Guieu et al., 2018; Massoth et al., 2007). Two shallow hydrothermal sites were investigated as part of the TONGA cruise (Guieu and Bonnet, 2019), revealing an 80-fold enrichment of DFe concentrations (< 0.45 µm) above the source relative to unimpacted waters of the WTSP (Tilliette et al., 2022). Despite their decrease towards the surface, elevated concentrations (0.6-10 nmol L^{-1}) persisted in the photic layer (0-150 m) allowing to sustain high rates of primary production. Although the effects of such hydrothermal fertilization on biological

activity are beginning to be elucidated on short temporal scales (Tilliette et al., in rev.), its effects on the biogeochemical signature of the exported and sedimented particles on larger temporal and spatial scales remain unclear.

Sediment traps are classically used to explore biogeochemical cycles in the ocean and since pioneering studies (e.g., Deuser, 1987; Deuser and Ross, 1980; Honjo et al., 1992), these devices have shown their potential to highlight the variability of the composition and fluxes of biological material in relation to surface productivity, depth or season. On their descent, in particular in the mesopelagic zone (200-1000 m), biological particles are subjected to intense bacterial remineralization and grazing by zooplankton (Boyd and Trull, 2007; Ducklow et al., 2001; Volk and Hoffert, 2013). Only a minor proportion of this material will eventually reach the deep-sea (> 1000 m) and an even smaller proportion will be buried in seafloor sediments (Berger et al., 1989; Hüneke and Henrich, 2011).

In this study, we determined the composition (i.e., lithogenic, organic matter, calcium carbonate – $CaCO_3$ and opal) of sinking and sedimented particles at different spatial and temporal scales over a large area of the WTSP, including two sites located along the Tonga Arc. The aim was to better understand how hydrothermal activity influences this region, both in terms of hydrothermally-derived trace metal concentrations and their influence on biological activity, and how volcanic activity impacts the footprint of metal particles.

2 Material and methods

This study was conducted as part of the TONGA cruise (GEOTRACES GPpr14; Guieu and Bonnet, 2019) onboard the R/V L'Atalante from October 31 to December 5, 2019, along a 6100 km-long transect crossing the Lau Basin (*Fig. 1*). Two shallow hydrothermal sources were identified at depths of 200 and 300 m, respectively (Tilliette et al., 2022). Mooring lines were deployed west of these

sources (~15 km; stations 5 and 10) along the main current direction once the seafloor reached ~2000 m.

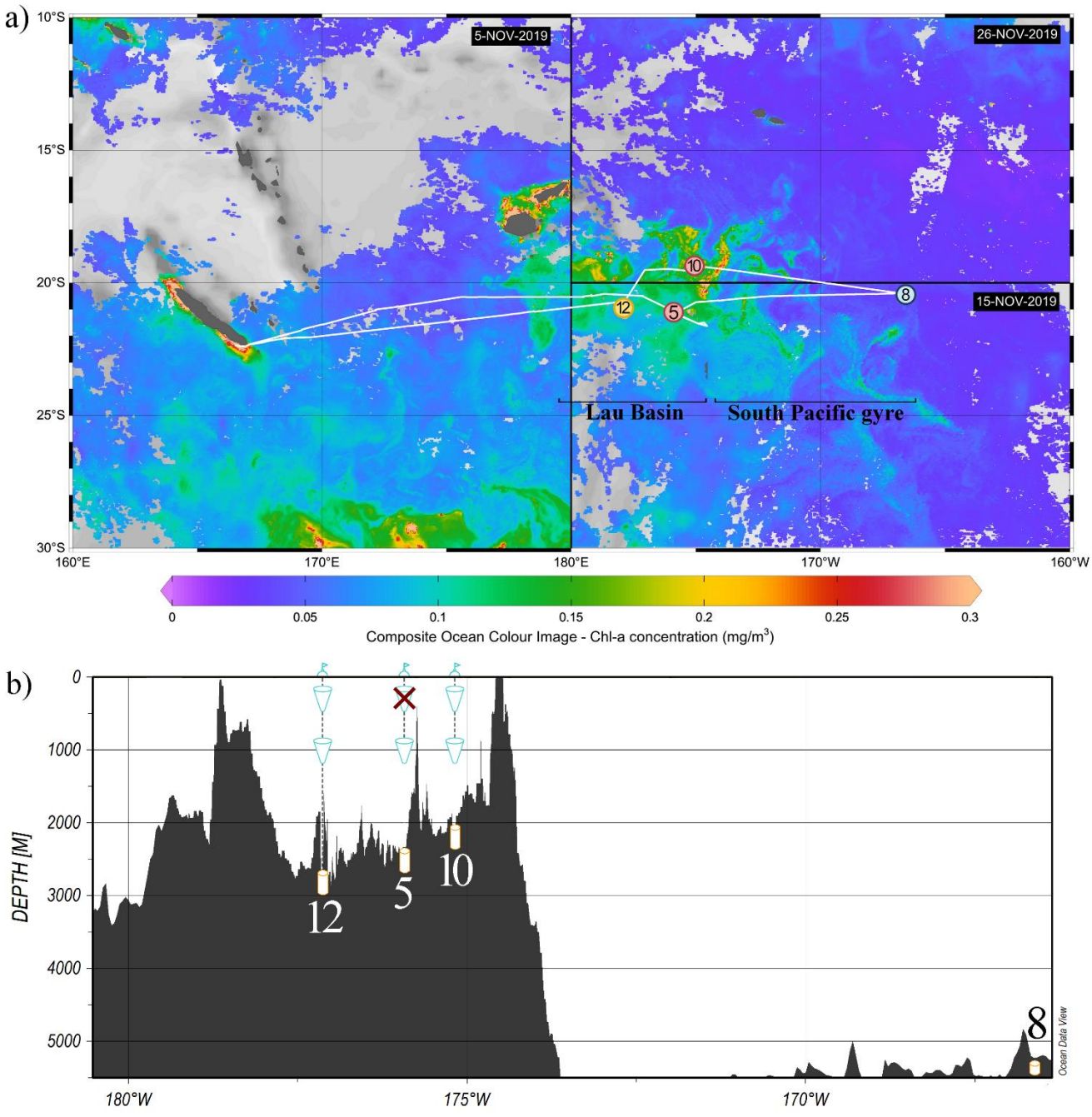

***Figure 1*. (a)** Cruise transect superimposed on surface chlorophyll-*a* concentrations (mg m^{-3}). Different oceanic regions were occupied during the cruise: the South Pacific gyre (station 8; sediment coring only) and the Lau Basin (stations 5 and 10), where a drifting mooring line was deployed for 5 and 4 days, respectively, as well as station 12 where a fixed mooring line was deployed for one year. Sediments were cored at each of these stations. Chlorophyll-*a* concentrations were derived from satellite images acquired during the respective period of occupancy: 5 November

2019 for the western part of the transect, 15 November for the southeastern part, and 29 November for the northeastern part. **(b)** Bathymetry along the cruise transect and instrumentation deployed at each station: sediment traps (cones) and sediment coring (cylinders).

2.1 Fieldwork

At stations 5 and 10, drifting conical sediment traps with a collection area of 1 m² (PPS-5, Technicap, France) were deployed at 200 and 1000 m on a surface-tethered drifter. Settling particles were collected at 24-h intervals for 5 days at station 5 (21°9.14' S, 175°44.42' W; November 10-14, 2019), and at 23-h intervals for 4 days at station 10 (19°24.54' S, 175°7.34' W; November 24-27, 2019). Unfortunately, due to a malfunction of the PPS-5 plate motor, no samples were collected at 200 m at station 5. At station 12 (20°42.41' S, 177°52.13' W), two PPS-5 were deployed at 200 and 1000 m on a fixed mooring line for one year (November 2019 to October 2020, sampling interval: 14 days). The fixed mooring line was equipped with two inclinometers (NKE S2IP) and two current meters (Nortek Aquadopp) placed at 222 and 1030 m. The angles and velocities at both depths are shown in *Fig. S1*. Each collection cup was filled with a 5% buffered formaldehyde solution prepared with filtered *in-situ* seawater to prevent microbial degradation and swimmer grazing. After trap recovery, the cups were stored in the dark at 4 °C.

Sediment cores were collected using a MC-8/100 multi-corer (Oktopus GmbH, Kiel, Germany) at the mooring positions and at the deep-sea reference site (station 8; 20°23.33' S, 166°25.4' W; *Fig. 1*). The seafloor depth for each core is specified in *Table 1*. Immediately after collection, the first 16 cm of collected cores were sliced into 1 to 5 cm slices, depending on the stations (see *Fig. 3*) and frozen at -20 °C.

Table 1. Composition (wt.% – percentage by weight) and sedimentation rate of seafloor sediments at each station.

Station	Depth	$CaCO_3$	Opal	Organic matter	Lithogenic	Sedimentation rates
-	*m*			*wt.%*		*cm kyr^{-1}*
Station 5	2140	2 ± 1	9 ± 1	0.1 ± 0.03	90 ± 1	58 ± 10
Station 10	1930	4 ± 1	7 ± 1	0.1 ± 0.03	88 ± 3	47 ± 7
Station 12	1940	64 ± 1	13 ± 1	0.4 ± 0.1	23 ± 3	61 ± 6
Station 8	5326	0.3 ± 0.1	11 ± 0.1	0.6 ± 0.2	88 ± 2	58*

Note. Due to Ra enrichment of probable hydrothermal origin at station 8, the estimated sedimentation rate has been given as an indication only (see section 3.4).

2.2 Laboratory work

2.2.1 Elemental composition of sinking material and seafloor sediments

Sediment trap samples were processed by the "Cellule Pièges" (INSU-CNRS: https://www.imev-mer.fr/web/?p=526). For each sediment trap cup, swimmers were carefully removed with Teflon tweezers under a stereomicroscope (Leica Wild MZ8). Any visible material attached to the swimmers was removed whenever possible, to avoid biasing particle flux. Samples were then rinsed three times with 50 mL of MilliQ water to remove salts and lyophilized for seven days. The total weight (wt) of each sample was measured on a Sartorius precision balance (± 0.01 mg).

Seafloor sediment samples were thawed at room temperature and lyophilized for seven days.

Both seafloor sediments and sediment trap samples were then split in different pre-weighted aliquots (~10-20 mg) for various analyses. Total carbon was measured with a CHN elemental analyzer (2400 Series II CHNS/O, Perkin Elmer®; precision ± 0.3%). Particulate organic carbon (POC) was determined similarly, after particulate inorganic carbon (PIC) removal by acidification with 2 N hydrochloric acid. Biogenic (BSi) and lithogenic (LSi) silica measurements were performed after sodium hydroxide (NaOH) and hydrofluoric acid (HF) digestion following the exact protocol described by Mosseri et al. (2005) and adapted from Brzezinski and Nelson (1995). For each aliquot, BSi was initially dissolved by NaOH digestion at 95 °C for 5 h. LSi was then extracted from the same aliquot by HF digestion at room temperature for 48 h. For both digests, the dissolved silicic acid (DSi)

concentrations of the resulting solutions were analyzed according to Nelson et al. (1989) with a UV-Vis spectrophotometer (Analytikjena® Spector 250 plus). DSi concentrations were also measured in the supernatant of each trap cup to account for BSi dissolution during trap deployment and were added to the BSi value determined by digestion (Hurd, 1972; Nelson et al., 1995; Nelson and Brzezinski, 1997). Several aliquots of certified reference material (GBW: marine sediment, NRCC) were digested and analyzed under the same conditions, allowing validation of Si data. GBW standard analyses averaged 28.5 ± 0.5 wt.% total Si (BSi + LSi ; n = 12), which compares well with the community consensus concentrations of 25.2 ± 0.6 wt.%. Al, Ca, Cu, Fe, Mn, Ni, Pb, Si and Zn concentrations were measured by ICP-OES (Inductively-Coupled Plasma Optical Emission Spectrometry; Perkin-Elmer® Optima-8000) after acid digestion of ~20 mg particulate aliquots in Teflon vials by successive addition of (1) 1 mL of 65% nitric acid (HNO_3^-) followed by (2) 500 µL of 65% HNO_3^- and 500 µL HF. At each step, aliquots were heated at 150 °C for 5 h. Several reagent blanks and certified reference material (GBW) were digested and analyzed under the same conditions. Blanks were below or close to the detection limits of the instrument and the percentage recovery obtained for the certified materials indicated accurate digestion and quantitative analysis for all elements (*Table S1*).

Dry material collected in acrylic traps deployed at 1000 m on the drifting mooring line at Station 10 was filtered onto 0.2 µm polycarbonate filters, rinsed with distilled water and dried at room temperature. Filters were then coated with gold and observed using a Phenom scanning electron microscope at 10 kV.

2.2.2 Grain size distribution of seafloor sediments

Grain size of sediments was determined at the Centre de Formation et de Recherche sur les Environnements Méditerranéens (CEFREM; France) laboratory using a Malvern Mastersize 3000 laser granulometer (precision ± 3%). Prior to measurement, dry sediments were homogenized, diluted in distilled water in order to achieve the concentration required by the software (i.e., 5-20% obscuration)

and ultrasonicated for 5 minutes. Since the number distribution may underestimate the larger particles, a particle size distribution based on a spherical equivalent volume model was used. The size of a particle was then represented by the diameter of an equivalent sphere of equal volume.

2.2.3 Sedimentation rates of seafloor sediments

Sedimentation rates were determined using ^{210}Pb, a natural decay-product of ^{226}Ra with a half-life of 22.3 years. ^{210}Pb deposited at the seabed by sedimentation is referred to as ^{210}Pb in excess ($^{210}Pb_{XS}$) relative to that found within sediment. Considering constant flux and accumulation rate (Robbins and Edgington, 1975), sedimentation rates were derived from the decrease of $^{210}Pb_{XS}$ activities with depth according to the following formula:

$$[^{210}Pb_{XS}]_z = [^{210}Pb_{XS}]_0 * e^{\left(-z\frac{\lambda}{SAR}\right)} \quad (1)$$

with $[^{210}Pb_{XS}]_0$ and $[^{210}Pb_{XS}]_z$; the excess ^{210}Pb activities at the water-sediment interface and at depth *z*, respectively; λ, the nuclide decay constant and SAR, the sediment accumulation rate. The activities of ^{210}Pb and ^{226}Ra were determined at the Environnements et Paléoenvironnements Océaniques et Continentaux (EPOC; France) laboratory on dry sediments using a low background, high efficiency well-type gamma spectrometer (CANBERRA; Schmidt et al., 2014).

2.3 Composition of the exported particles and sediments

The elemental analyses described above were used to determine the four main fractions of the collected sinking and sedimented material: organic matter (OM), calcium carbonates ($CaCO_3$), opal and lithogenic. The OM fraction was calculated from POC concentrations as 2.199 × POC (Klaas and Archer, 2002). The $CaCO_3$ fraction was estimated from PIC as $CaCO_3$ = PIC × 8.33 (Verardo et al., 1990). PIC was preferentially used, as the method from Ca tended to overestimate the $CaCO_3$ fraction on some samples (> 100 wt.% of total collection weight; *Table S2*), likely due to the presence of

lithogenic Ca. The opal fraction was determined from BSi concentrations as Opal = BSi × 2.4 (Mortlock and Froelich, 1989). Finally, the lithogenic fraction was determined through the mass balance method (Wefer and Fischer, 1993), by subtracting the sum of the above three fractions from the total collection weight. This method was preferentially chosen in view of the potential bias of using lithogenic tracers (LSi or Al) in this region, as these two elements can be significantly enriched or depleted through volcanic or hydrothermal activity, as discussed in section 4.4.

2.4 Statistical analysis

To determine if significant differences could be observed in the fractions of material collected at the different stations, a non-parametric Mann-Whitney test was performed. This two-tailed distribution-free test was selected due to the non-normally distributed data, previously determined through a Kolmogorov-Smirnov test. Differences were considered significant at a p-value (p) < 0.05.

3 Results

3.1 Composition of the sinking particles and sediments

3.1.1 Biogenic particles

Three fractions of the collected material can be used as proxies for biological production: $CaCO_3$, opal and OM.

Exported particles. $CaCO_3$ was the most abundant biogenic component of the exported material (on average over stations and depths: 52-58 wt.%; *Fig. S2*) if station 10 at 1000 m is excluded (average 17 wt.%). The amount of $CaCO_3$ collected averaged 9 ± 1 mg d^{-1} at all stations and depths, with a significantly higher accumulation at stations 5 and 10 at 1000 m (~34 ± 15 mg d^{-1}; $p < 0.05$; *Fig. 2*). At station 12 (fixed mooring), only two $CaCO_3$ peaks were observed at 1000 m (in December and February) while they were more frequent at 200 m. Opal fraction was the smallest biogenic component of the sinking material (1-5 wt.%; *Fig. S2*), regardless of station and collection depth (~1.2 ± 1.6 mg d^{-1}; *Fig. 2*), with a significantly higher quantity collected at 1000 m than at 200 m ($p < 0.05$). Two opal

peaks, matching the $CaCO_3$ peaks in December and February, were observed at 1000 m at the fixed mooring station (station 12). OM fraction was the second most abundant biogenic component at 200 m (31-41 wt.%; *Fig. S2*), with similar amounts of material collected at all stations (~5.3 ± 2.6 mg d^{-1}, $p = 0.34$, *Fig. 2*). Apart from station 12 (~3 ± 2.5 mg d^{-1}; $p = 0.01$), OM collected at 1000 m (~6.6 ± 1.8 mg d^{-1}; 4-22 wt.%) did not significantly differ from those collected at 200 m ($p > 0.1$). Amounts collected at station 12 at 1000 m were significantly lower than at station 10 at the same depth ($p = 0.01$). OM peaks were observed from December to May in both traps of station 12. At 1000 m, those peaks matched those of opal and $CaCO_3$.

Seafloor sediments. The proportion of $CaCO_3$ in seafloor sediments was very low (< 5 wt.%) at most stations, except at station 12 (64 ± 1 wt.%, $p < 0.05$, *Table 1*). Although present in low proportions (10 ± 2 wt.%), opal was the most abundant biogenic component in seafloor sediments, with no difference between stations ($p > 0.05$). OM proportion was less than 1 wt.% for all stations and did not differ between stations ($p > 0.05$).

3.1.2 Lithogenic material

Exported particles. The smallest amount of lithogenic material was collected at 200 m at station 10 (~0.5 ± 0.2 mg d^{-1}; 3 ± 1 wt.%; *Figs. 2 and S2*). In contrast, at the same station at 1000 m, the lithogenic material was up to four orders of magnitude higher (maximum of 344 mg d^{-1}; 75 ± 3 wt.%). Large amounts were also collected at 1000 m at station 5 (~16 ± 4 mg d^{-1}; 33 ± 11 wt.%), albeit significantly lower (by a factor of 20, $p = 0.03$). In comparison, at station 12 (fixed mooring), lithogenic amounts were lower throughout the year ($p < 0.02$) and of the same order of magnitude in both traps (~2.6 ± 1.9 mg d^{-1}; 16 ± 7 wt.%; $p = 0.2$). At 200 m at station 12, the observed lithogenic peaks coincided with most OM peaks. Notably, two lithogenic peaks (up to 14 mg d^{-1}), matching those of all biogenic components ($CaCO_3$, opal, OM), were observed in December and February at 1000 m.

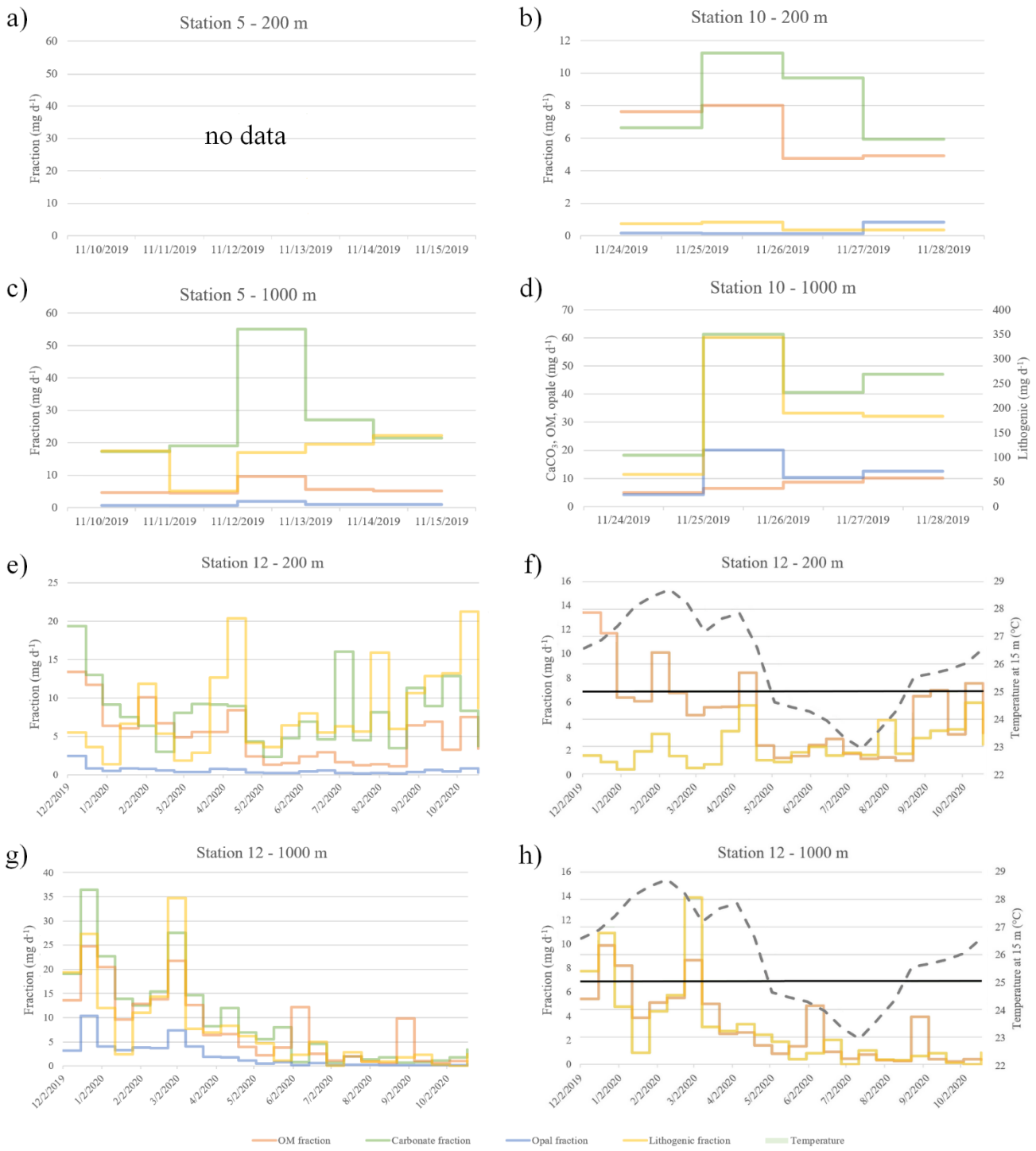

Figure 2. Temporal dynamics of exported material (mg d^{-1}) in drifting **(a-d)** and fixed **(e-h)** sediment traps: organic matter (orange line), calcium carbonate (green line), opal (blue line) and lithogenic fraction (yellow line). Shown on the different panels are: station 5 at 200 and 1000 m **(a, c)**, station 10 at 200 and 1000 m **(b, d)** and station 12 at 200 and 1000 m **(e, g)**. *Note that the lithogenic fraction is represented on a different y-label for station 10 – 1000 m* ***(c)***. Panels **(f)** and **(h)**: organic and lithogenic material (left y-label) versus temperature at 15 m (right y-label; grey dotted line) for both traps at station 12. The black line delineates a temperature of 25 °C. Temperature data were extracted

from the World Ocean Atlas database (Locarnini et al., 2018): average (2005-2017) at 15 m, near station 12. Cumulative histograms of these fractions are shown in *Fig. S2*.

Seafloor sediments. The lithogenic fraction was the most abundant fraction in the seafloor sediments at stations 5, 8 and 10 (88-90 wt.%, *Table 1*). In contrast, at station 12, the lithogenic fraction was only 23 ± 3 wt.% ($p < 0.001$), due to the dilution effect by the high $CaCO_3$ fraction.

3.2 Trace metal content and enrichment factors

Particulate metals measured in sinking particles and in seafloor sediments are presented in *Figs. S3* and *S4*.

The bulk metal composition was corrected for biogenic calcium carbonate content, following the approach described by German et al. (1997). Indeed, as $CaCO_3$ contains very low levels of trace elements, it can dilute the metal contribution of the collected material. Prior to any interpretation, the concentration of an element (E) was corrected on a calcium carbonate-free basis (*cfb*) following:

$$[E]_{cfb} = \frac{[E]}{(100 - \%CaCO_3)} \quad (2)$$

The metal content of sinking and sedimented material was compared to the concentrations of reference pelagic clays sampled in the Pacific Ocean ("pc"; *Table 2*; Li and Schoonmaker, 2003; Sayles and Bischoff, 1973) using two distinct methods: enrichments factors (EF) and metal excess (XS).

EF in exported material. For the sinking material, EF were calculated by normalizing the concentration ratio of an element $(E)_{cfb}$ to aluminum (Al_{cfb}, lithogenic tracer) to the same elemental ratio measured in pelagic clays following the formula:

$$E_{EF} = \frac{[E]_{cfb\ sample}/[Al]_{cfb\ sample}}{[E]_{pc}/[Al]_{pc}} \quad (3)$$

Enrichment of Zn (Zn_{EF}) was detected in the material collected from all sediment traps compared to reference pelagic clays (x6-39; *Table 2*), except at 1000 m at station 10. Slightly elevated Fe_{EF} was estimated at 1000 m at stations 5 and 12 (x1.5-1.8). No Mn_{EF} was detected in traps, except at 200 m at station 10 (x7). Significant Ni_{EF} (x3-7) were observed at 1000 m at station 12 and at 200 m at station 10. Cu_{EF} was measured only in the material collected at station 10 at 200 m and station 12 at 1000 m (x18 and x2, respectively). LSi_{EF} was estimated at 1000 m at all stations, up to a factor of 14 (station 10).

Table 2. Elemental enrichment factors (E_{EF}) of metals in sinking material relative to aluminum (Al_{cfb}) and average concentrations in reference pelagic clays.

Sample	Fe	Mn	Cu	Zn	Ni	LSi
Station 5 - 1000 m	**1.4**	*0.2*	*0.6*	**11**	1.1	**5.2**
Station 10 - 200 m	1.1	**5.0**	**18**	**37**	**7.3**	*0.4*
Station 10 - 1000 m	1.0	*0.01*	*0.03*	*0.7*	*0.1*	**14**
Station 12 - 200 m	1.1	*0.02*	*0.2*	**6.1**	*0.1*	*0.2*
Station 12 - 1000 m	**1.7**	*0.6*	**2.0**	**39**	**2.7**	**1.6**
Reference pelagic clays	5.9 ± 0.6	1.1 ± 0.4	469 ± 181	158 ± 12	196 ± 14	25 ± 1

Note. Enrichments relative to Pacific Ocean pelagic clays (EF > 1) are shown in bold while depletions relative to the reference (EF < 1) are shown in italics. Average concentrations and standard deviations (in wt.% for Fe, Mn and LSi and ppm for Cu, Zn and Ni) within several reference pelagic clays (from Li and Schoonmaker, 2003; Sayles and Bischoff, 1973; Taylor and McLennan, 1985) are shown at the bottom of the table. Note that the range of concentrations measured for each element in these references provides only a rough estimate of metal non-detrital enrichment in the material collected in this study. It may therefore over- or underestimate the magnitude of these enrichments.

Elemental excess in seafloor sediments. For seafloor sediments, metal excess relative to reference pelagic clay composition was determined by correcting $[E]_{cfb}$ for detrital inputs (German et al., 1997) assuming that this reference material was representative of a deep-sea detrital end-member. Detrital concentrations of each element were calculated according to:

$$[E]_{det} = [Al]_{cfb} * \frac{[E]_{pc}}{[Al]_{pc}} \quad (4)$$

288 It is important to note that this calculation assumes that all sedimentary Al originates from detrital
289 material. However, sedimentary Al concentrations could originate from both hydrothermal and detrital
290 sources (Massoth et al., 1998; Resing and Sansone, 1999; Von Damm, 1990). Consequently, Al
291 *normalization* may have underestimated the extent of hydrothermal enrichment in our seafloor
292 sediments (Chavagnac et al., 2008). That fraction of non-detrital origin, denoted $[E]_{XS}$, was determined
293 by subtracting $[E]_{det}$ from $[E]_{cfb}$.

294 Several metals were in excess in the sampled sediments relative to the composition of reference pelagic
295 clays of the Pacific (*Fig. 3*). At all depths, sediments showed marked Fe_{XS}, although significantly lower
296 at station 8 (on average ~3 wt.% Fe_{XS}, $p < 0.05$) than at stations located in the Lau Basin (up to ~5
297 wt.% Fe_{XS}). Significant Mn_{XS} (~2-18 wt.%) and Cu_{XS} (~100-230 ppm) were detected in all sediments,
298 with the highest excess measured at station 12 ($p < 0.05$). This station also had the unique characteristic
299 of displaying Ni_{XS} (~100 ppm), Zn_{XS} (~10 ppm) and Pb_{XS} (~20 ppm) while no excess was detected at
300 the other stations (excluding small occasional Pb_{XS} within the station 8 profile; up to 10 ppm). High
301 LSi_{XS} were measured at stations 5 (~5 wt.%) and 10 (up to ~7 wt.%).

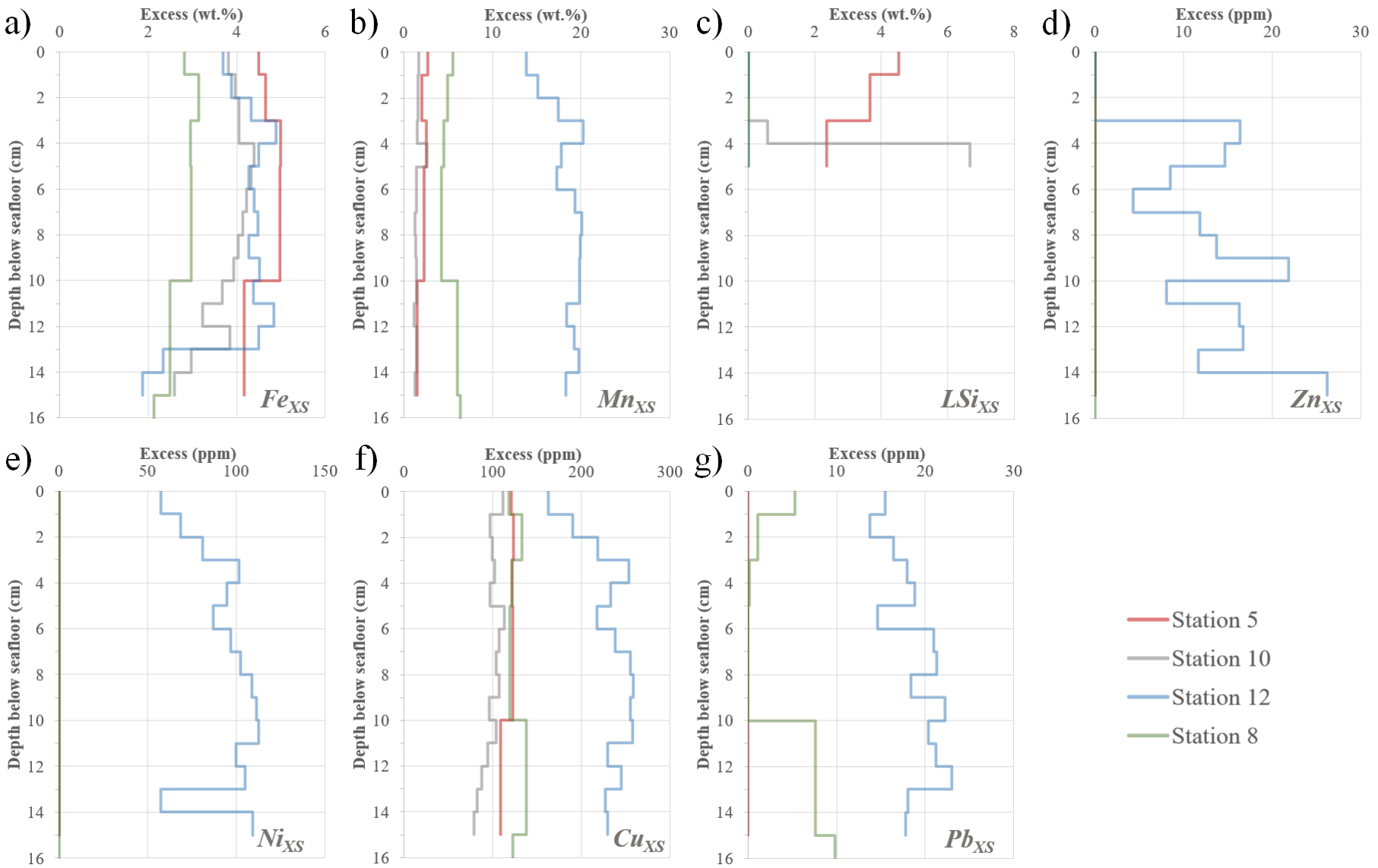

Figure 3. Excess of metal (E_{XS}) in each slice of seafloor sediments relative to the composition of reference pelagic clays: **(a)** iron (Fe_{XS}), **(b)** manganese (Mn_{XS}), **(c)** lithogenic silica (LSi_{XS}), **(d)** zinc (Zn_{XS}), **(e)** nickel (Ni_{XS}), **(f)** copper (Cu_{XS}) and **(g)** lead (Pb_{XS}). Excess in major elements are represented in wt.% (Fe, Mn, Si, Ca) and minor elements (Zn, Ni, Cu, Pb) in ppm.

3.3 Grain size distribution of seafloor sediments

The smallest particle sizes, mainly between 2 and 16 µm, were measured at station 8 (*Fig. 4*). Larger particles were identified at stations 5 and 10, primarily between 30 and 110 µm. A wide range of particle sizes was measured at station 12, mainly ranging from 1 to 310 µm and up to 976 µm.

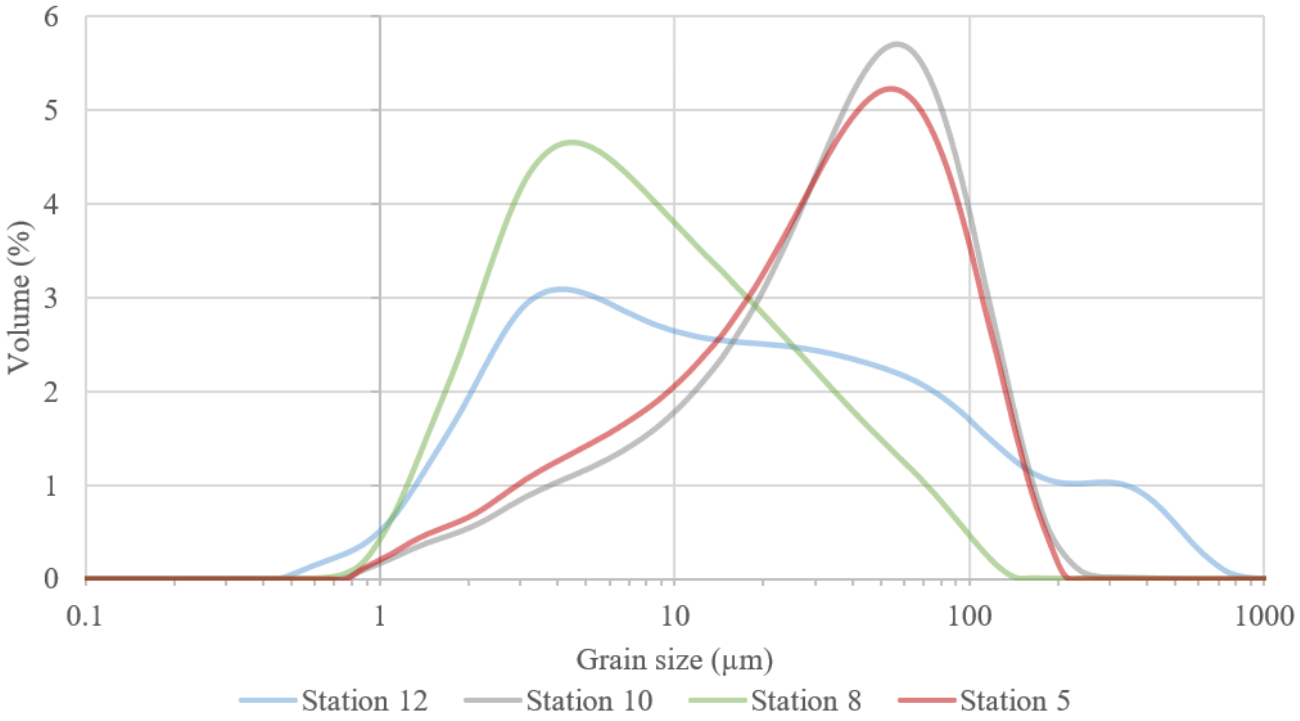

Figure 4. Grain size distribution averaged for all sediment slices at each station. The distribution for each sediment slice is shown in *Figure S5*.

3.4 Sedimentation rate of seafloor sediments

^{210}Pb and $^{210}Pb_{XS}$ activities ranged from 11 to 290 mBq g^{-1} and from 1 to 259 mBq g^{-1}, respectively (*Fig. S6*). Values of $^{210}Pb_{XS}$ decreased exponentially with depth in the sediments cored at stations 5, 10 and 12, reaching negligible levels at about 6 to 10 cm, depending on the core considered. This was not the case for core 8, which still exhibited high $^{210}Pb_{XS}$ in the 10-15 cm sediment layer, associated with the highest ^{226}Ra values measured in the studied cores (100-200 mBq^{-1}). Such high ^{226}Ra activities may be related to hydrothermal enrichment. Indeed, it could be suspected that below 3-5 cm, total ^{210}Pb activities correspond to a combination of $^{210}Pb_{XS}$ and ^{210}Pb ingrowth from Ra enrichment: the deepest

$^{210}Pb_{XS}$ activities are then not reliable to estimate the sedimentation accumulation rate. For stations 5, 10 and 12, sediment accumulation rates ranged from 47 to 61 cm kyr^{-1} (*Table 1*). For station 8, considering only the first two levels of the profile, it was possible to calculate a sedimentation rate of 58 cm kyr^{-1}, close to those obtained at the other stations.

4 Discussion

4.1 Potential biases of sediment traps

Sediment traps have been a standard tool for measuring sinking particle fluxes for decades, yet uncertainties remain regarding their collection efficiency (e.g., Baker et al., 2020; Buesseler et al., 2007; Butman, 1986; Gardner, 1980; Hargrave and Burns, 1979). Advantages of these instruments include their unequivocal separation of sinking material from suspended one, proper preservation of samples for laboratory analyses and accurate sampling periods. Disadvantages include their potential hydrodynamic effects, short collection time-scales (for drifting lines), possible contamination by swimmers and attachment of non-swimming material on them (Buesseler et al., 2007). Such biases could result in under- or over-trapping. Field comparison of different trap designs provided valuable insight into the appropriate procedures for these tools (Baker et al., 2020; Gardner, 1980; Scholten et al., 2001 and references therein). In the present study, efforts were employed to accurately collect sinking particles by **(1)** ensuring that traps were deployed below the mixed layer (Owens et al., 2013), **(2)** focusing the discussion on collected relative weights and elemental ratios rather than material fluxes, and **(3)** unhooking any visible material attached to swimmers whenever possible before removal. Furthermore, the deployment position of the fixed mooring line (i.e., station 12) was predetermined by Ariane modeling simulations (Grima and Maes, pers. comm., 2019) to minimize the impact of regional dynamics features (e.g., current velocities and physical dynamics that can drag the mooring line, tilt the trap or cause upward motions). Although we are aware of these biases, sediment traps remain the only way to collect free-sinking particles from the suspended pool, and fixed traps are

345 the only tool capable of collecting free-sinking material annually in a specific region. The physical
346 conditions of the fixed sediment traps at different deployment depths are described in *Text S1*.

347 **4.2 Non-vertical sinking of particles collected in the fixed sediment trap**

348 The peaks of the different fractions composing the material were not simultaneously observed in the
349 traps deployed at 200 and 1000 m at the same site (*Fig. 2*). The temporal shift of these peaks would
350 indicate that particles would be collected at 1000 m, 30 to 56 days after being collected at 200 m. This
351 observation suggests that while sinking toward the seafloor, the particles were subject to horizontal
352 transport, in view of the westward main current (Tilliette et al., 2022). Thus, the collected particles
353 sank progressively from the photic layer near the arc (0-150 m) while being horizontally advected
354 toward the location of the fixed mooring. The time lag between the collection at 200 and 1000 m is due
355 to depth-dependent physical dynamics (faster current velocity at surface and influence of mesoscale
356 structures predominant in the sub-region; Rousselet et al., 2018) as well as the travel time of the water
357 masses, much faster at 200 m than at 1000 m. Indeed, Lagrangian simulations through Ariane software
358 showed that sinking particles from the Tonga Arc require 61 and 103 days to reach the fixed trap site
359 at 200 and 1000 m, respectively (Grima, pers. comm., 2022). This is consistent with the time lag
360 between the observed peaks at 200 and 1000 m (e.g., current velocities and physical dynamics that can
361 drag the mooring line, tilt the trap or cause upward motions). These longer transport times (> one
362 month) of particles collected at 1000 m may also explain the larger amounts of particles collected in
363 some cases at depth. This reasoning suggests that an important portion of the sinking material collected
364 in the sediment traps at station 12 would originate from the photic layer near the Tonga Arc, influenced
365 by shallow hydrothermal fluids, as discussed later in this manuscript. Nevertheless, the finding of a
366 non-vertical sinking of suspended particles highlights the importance of employing numerous
367 precautions when interpreting sediment trap data, especially when estimating POC transfer efficiency,
368 which would then be completely spurious in such a case.

4.3 Biogenic components of sinking particles and seafloor sediments

4.3.1 Summary of production at studied stations during austral summer conditions

During the TONGA cruise in the austral summer (Bonnet, pers. comm., 2022), high rates of primary production (PP) were estimated in the Lau Basin (up to 145 mmol C m^{-2} yr^{-1} at station 10; *Table S3*). This production was largely supported by cyanobacteria (~70% of total chlorophyll-*a*), primarily diazotrophs such as *Trichodesmium* that led to high N_2 fixation rates (up to 2727 µmol N m^{-2} d^{-1} at station 5). A significant contribution of coccolithophores was also estimated (~25%) while diatoms and dinoflagellates represented less than 10% of total chlorophyll-*a* in the Lau Basin. In comparison, PP and N_2 fixation were much lower at station 8 (< 35 mmol C m^{-2} d^{-1} and 225 µmol N m^{-2} d^{-1}, respectively) and supported predominantly by non-diazotrophic cyanobacteria (Bonnet et al., in rev.).

4.3.2 Calcium carbonate

In the ocean, the dominant source of $CaCO_3$ (mainly calcite) comes from a wide variety of pelagic organisms such as coccolithophores and foraminifera (Morse et al., 2007). In the sediment traps, high $CaCO_3$ contents were measured at all stations, regardless of depth (200 m: 16-82 wt.%, 1000 m: 12-93 wt.%; *Fig. S2*), consistent with the high productivity of the Lau Basin (*Table S3*). High levels of $CaCO_3$ were also measured in the sediments at station 12 (~64 wt.%), in agreement with values reported in the literature from the region (Zhang et al., 2022), suggesting good preservation of the sinking material on the seafloor. In contrast, the percentage of $CaCO_3$ in the seafloor sediments at stations 5, 8 and 10 was considerably lower (0.3-4 wt.%; *Table 1*). The low $CaCO_3$ preservation at station 8 can easily be explained by the seafloor depth (5326 m), far below the calcite compensation depth (CCD; *Fig. S7*). Conversely, the seafloor at stations 5 and 10 (~2000 m), located above the lysocline and therefore the CCD, cannot explain the observed patterns. As the Tonga Arc harbors an intense hydrothermal activity (see section 1), its seafloor may be characterized by strong physical and chemical gradients (temperature, oxygen levels, multiple forms of chemical energy) and encompass a diverse range of habitats for microbial life (Karl, 1995). It would thus harbor enormous biomasses and productivities

394 relative to other regions of the deep ocean (Zierenberg et al., 2000), which may explain the low $CaCO_3$
395 content of the sediments at stations 5 and 10.

396 *4.3.3 Opal*

397 In the ocean, opal minerals originate from a wide variety of silica-skeleton organisms, primarily
398 diatoms, radiolarians but also silicoflagellates to a lesser extent (Tréguer et al., 1995). The opal fraction
399 was the least abundant fraction in the sinking material (1-5 wt.%; *Fig. S2*), in agreement with the low
400 contribution of diatoms to total chlorophyll-*a* in the Lau Basin during the TONGA cruise (*Table S3*).
401 Interestingly, more opal was collected at 1000 m than at 200 m (~2.2 ± 2.5 and ~0.15 ± 0.01 mg d^{-1},
402 respectively). As discussed in Section 4.2, such a finding can be explained by the time lag of particle
403 arrival at 200 and 1000 m, combined with the fast sinking rates of opal skeletons (Bodungen et al.,
404 2013; Turner, 2002). In comparison with the sediment traps, a greater proportion of opal was found in
405 the seafloor sediments, with similar proportions at all stations (6-13 wt.%; *Table 1*). Since BSi is known
406 to have a higher preservation efficiency than OM and $CaCO_3$, degradation of these other fractions may
407 therefore account for the increasing proportion of opal in sediments (Emerson and Hedges, 1988;
408 Gersonde et al., 2005). Furthermore, opal sinks at rates fast enough to contribute significantly to
409 seafloor sediments in contrast to other biogenic fractions (Sarmiento and Gruber, 2006).

410 *4.3.4 Organic matter*

411 The abundant proportion of OM collected in all traps (8-73 wt.%; *Fig. S2*) can easily be linked to the
412 Lau Basin productivity, which hosts shallow hydrothermal sources driving a ~360,000 km^2
413 productivity hotspot, mainly supported by diazotrophs such as *Trichodesmium* (up to 84% of total
414 export measured during the cruise; Bonnet et al., in rev.). In addition, exported POC amounts were
415 higher at stations near shallow hydrothermal sources (i.e., stations 5 and 10) than at station 12, where
416 the impact of shallow hydrothermalism is less evident. This finding supports the contribution of
417 hydrothermal supply in driving the high productivity of the Lau Basin.

Strong seasonality of OM was observed at station 12 with peaks occurring from December to April and August to November (except at 1000 m for the latter period). Interestingly, this large export of OM matched well with the export of lithogenic material, except for the April to August period when little OM was exported, despite the high supply of lithogenic material (up to 4.5 mg d^{-1}). This is probably related to the thermal fitness of *Trichodesmium*, which only grows at temperatures > 25 °C (Carpenter and Capone, 1992), reached in the Lau Basin between September and April (*Fig. 2f, h*). Thus, the high amount of OM exported in the Lau Basin appears to be dependent on lithogenic-derived nutrient inputs, suggesting that this material, most likely of hydrothermal origin (Tilliette et al., 2022), would drive the high diazotroph-mediated production. In seafloor sediments, as expected, only a minor proportion of OM was sequestrated (0.1-0.6%; Berger et al., 1989; Hüneke and Henrich, 2011), as most of this material is remineralized during its transport to the deep ocean (Boyd and Trull, 2007 and reference therein).

4.4 Origin and characteristics of the metallic component in sinking and sedimented particles

Table 3. Average Boström indexes measured in sinking material and seafloor sediments for each station.

Station	Depth	Boström index	
-	*(m)*	*mean*	*sd*
Station 5	1000	50.6	0.4
	Seafloor	39.7	1.7
Station 10	200	23.8	6.1
	1000	66.6	0.5
	Seafloor	45.2	1.3
Station 12	200	55.6	9.7
	1000	42.7	6.0
	Seafloor	15.9	0.9
Station 8	Seafloor	37.8	1.0

Note. Indexes were measured as follows: $100^{x}[Al_{cfb}/(Al_{cfb}+Mn_{cfb}+Fe_{cfb})]$ (Boström et al., 1969). The index for detrital pelagic sediments is 66 (Kyte et al., 1993; Plank et al., 2007). An index below 45 reflects fallout from a dispersed hydrothermal plume, having a high contribution of Fe-Mn oxides mixed with decreasing proportions of detrital material as distance from the source decreases (Chavagnac et al., 2008; Dymond, 1981). An index below 15 reflects near-vent sulfide debris (Mills et al., 1993). The set of index values in each trap cup and sediment slice is available in the supplementary material (*Table S4*).

As described in Section 3.2, the collected material was highly enriched in several metals compared to reference pelagic clays, most likely originating from the Tonga Arc area (see Section 4.2). Given the preponderance of shallow and deep hydrothermal sources in the Lau Basin on and between the Tonga Tofua Arc and the Lau and Tonga ridges (e.g., Anderson et al., 2021; Baker et al., 2019; Beaulieu and Szafrański, 2020; Lupton et al., 2004; Massoth et al., 2007; Tilliette et al., 2022), the question of the origin of this metal excess is of upmost interest. Hydrothermal material has a particular signature characterized by low Al content but rich in Fe and Mn, as well as many other metals such as Cu, Zn, Ni and Pb (Boström et al., 1969; Boström and Peterson, 1969; Cronan, 1972). However, particularities exist for these elements, as some of them, such as Cu and especially Ni and Zn, decrease dramatically with distance from the source relative to Fe, due to their rapid removal by sulfide-bearing phases (Trocine and Trefry, 1988). A convenient way to discriminate material of hydrothermal origin is based on the Boström index using Al_{cfb}, Fe_{cfb} and Mn_{cfb} concentrations (Boström et al., 1969). Its value provides a clear indication of the material provenance: a value close to 66 would indicate a clastic detrital sediment (Kyte et al., 1993; Plank et al., 2007) while values < 45 would indicate a significant hydrothermal component (Chavagnac et al., 2005; Humphris et al., 1995; Mills and Elderfield, 1995). The closer the value is to 0, the more hydrothermal the material is and thus a much closer location to the hydrothermal source (Dymond, 1981; Mills et al., 1993). In this study, indexes with particular and diverse signatures were determined, suggesting the presence of hydrothermal sources, remote or not, at some of the stations studied (*Table 3*).

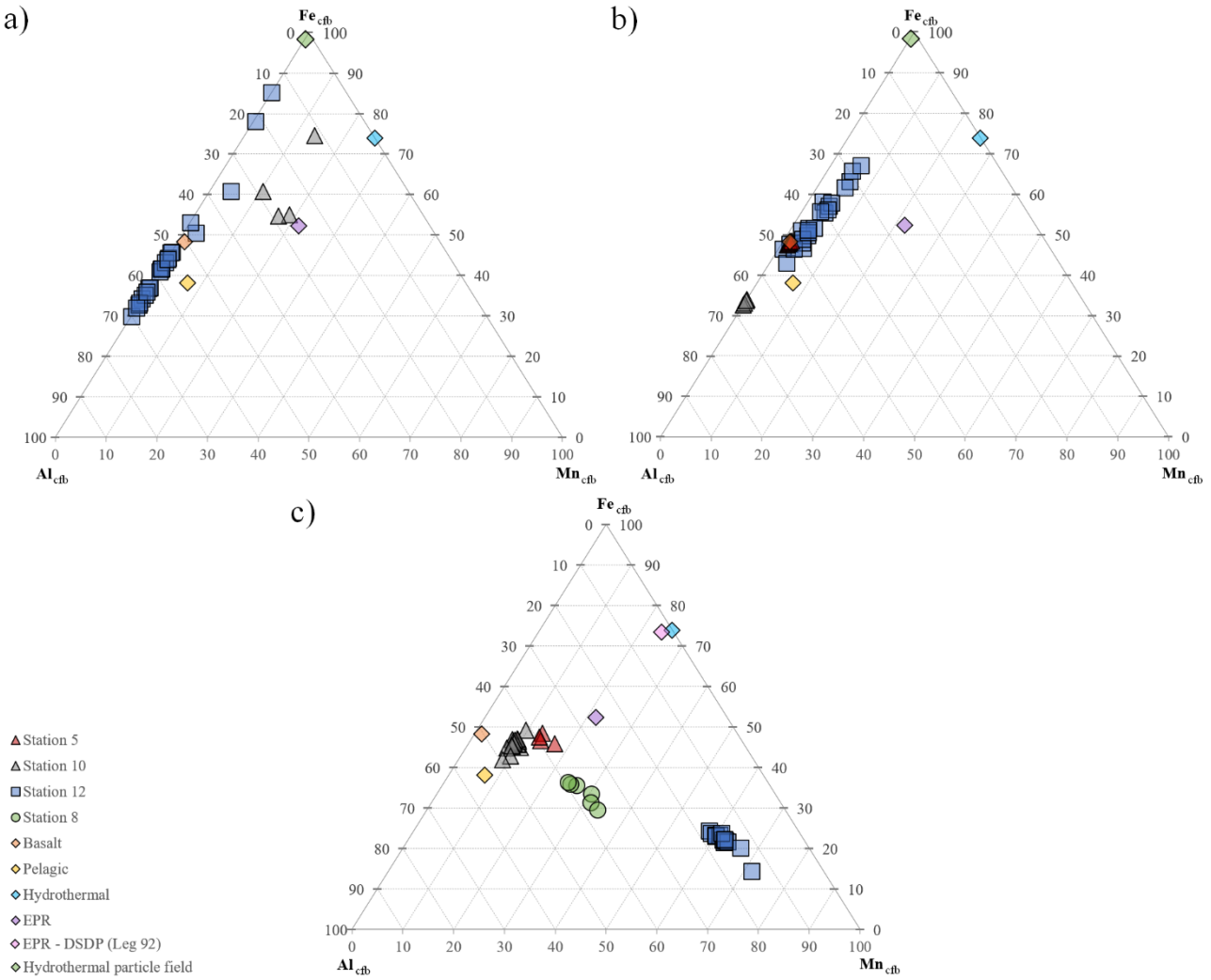

Figure 5. Fe_{cfb}, Mn_{cfb} and Al_{cfb} ternary diagrams for sinking material collected at **(a)** 200 m and **(b)** 1000 m and for **(c)** seafloor sediments. Also shown for comparison are some reference materials such as basalt (Japan Basalt, GSJ; Imai et al., 1995), reference pelagic clays (see *Table 2*), a hydrothermal vent solution (Li and Schoonmaker, 2003), a reference sedimentary material from the East Pacific Rise (EPR; Barrett et al., 2021; Nohara and Yokoto, 1978) and a hydrothermal particle field (Edmonds and German, 2004).

4.4.1 Along the Tonga Arc (small scale)

Stations 5 and 10 are located along the Tonga Arc, which hosts a multitude of active hydrothermal vents (e.g., Beaulieu and Szafrański, 2020; Lupton et al., 2004; Massoth et al., 2007). About 15 km from the location of each of the drifting mooring lines, a shallow hydrothermal source was identified during the TONGA cruise: at ~200 m at station 5 and at ~300 m at station 10 (Tilliette et al., 2022).

Station 10 revealed materials with distinctive signatures depending on sampling depth. At 200 m, a low Boström index was estimated at 24 ± 6 with Fe-Mn-rich material (*Table 3*, *Fig. 5a*). For comparison, metalliferous sediments collected from two to 25 km downstream of the Rain hydrothermal vent on the Mid-Atlantic ridge display similar Böstrom values of ~25 (Cave et al., 2002). Such index values obtained for our samples is a clear signature of a fairly close hydrothermal source, in agreement with the identification of a shallow source (~300 m) ~15 km away from the drifting mooring initial position, showing multiple acoustic anomalies and high DFe concentrations (Tilliette et al., 2022). Consistently, Cu_{EF}, Zn_{EF} and Ni_{EF} were detected in the trap (x18, 37 and 7, respectively; *Table 2*), compared to reference pelagic clays. It should be noted that biological (intracellular) inputs through organic matter (~41 wt.%) must contribute in part to these high enrichments relative to reference pelagic clays, since some metals, notably Zn, are highly abundant in phytoplankton ($[C_{106}N_{16}P_1]_{1000}Fe_{11.9}Zn_{1.27}Cu_{0.15}$; Ho et al., 2003; Redfield et al., 1963; Zhang et al., 2018). However, based on these elemental ratios, the biological fraction would represent only a small part of the total Zn concentration (~3%). At 1000 m, a Boström index typical of conventional detrital material was measured (*Table 3*), although the Al-Fe-Mn signature of the collected material seems to differ from that of the reference pelagic clays (*Fig. 5b*). Yet, station 10 is located close to the Late'iki submarine volcano, which was erupted a month prior to the cruise. This surtseyan eruption created a new island, baptized New Late'iki, which eroded in just two months. This erosion released a large amount of volcanic material into the water column, which was detectable until December 2020 (Plank et al., 2020). Accordingly, a huge abundance of basaltic glass, likely from this eruption, was collected in the 1000 m-trap deployed at this station (*Fig. 6*), the quantity of lithogenic material being impressive (196 ± 74 mg d^{-1}; *Fig. 2c*). Indeed, the angular shape of this volcanic material indicates its recent origin and freshness rather than remobilized volcanic particles, which would display more rounded angles. The higher Boström index at 1000 m (~40 to 66; *Table 3*) can therefore be attributed to the predominance of volcanic-derived particles, a material reported as Mn-poor but Fe and Al-rich (*Fig. 5b*; e.g., Almirón

et al., 2021; Fiantis et al., 2010; Leonelli et al., 2007; Naji and Asi, 2008; Oskarasson, 2010; Razzhigaeva et al., 2009; Tchakoute Kouamo et al., 2012). It also explains the high estimated LSi_{EF} at 1000 m (x14 relative to reference pelagic clays) as this element has been reported to be enriched in volcanic material relative to pelagic ones (Li and Schoonmaker, 2003; Sayles and Bischoff, 1973; Bailey, 1993; Fiantis et al., 2010). Thus, a mixture of volcanic, hydrothermal and detrital material probably prevailed at 1000 m. In the seafloor sediments, a moderate index (45 ± 1 over the whole core; *Table 3*) reflected the presence of metals fed by a rather distal hydrothermal source providing high Fe, Cu and, to a lesser extent, Mn contents (*Figs. 3*, *5c*). Indeed, in addition to the near-surface hydrothermal source, deep sources are likely to occur (Tilliette et al., 2022) within a reasonable distance of the station given the particle size (~80 µm), typical of distal transport (Feely et al., 1990, 1987; Lou et al., 2020). Consistently, estimated sedimentation rates were 94-470 times higher than those of pelagic sediments (average 0.1-0.5 mm kyr^{-1}; Li and Schoonmaker, 2003; Piper, 2005) and in the range of those measured in coastal areas, continental margins and hydrothermally-influenced areas accumulating to several cm kyr^{-1} (Cave, 2002; Cave et al., 2002; Dutkiewicz et al., 2016; Mahiques et al., 2011). This indicates a much greater material flux, likely from shallow and deep hydrothermal sources. The volcanic signature identified at 1000 m was recovered at different depths in the sediments of this station, with LSi_{XS} of 6.7 wt.%, but also at station 5 (up to 4.5 wt.% LSi_{XS}). This result was not surprising as this volcano is known to have recurrent eruptions since the 18^{th} century (Ewart et al., 1977), consistent with the LSi_{XS} found in cored sediments at station 10 (depths > 3 cm below the seafloor, corresponding to the 18th century; see *Table 1*).

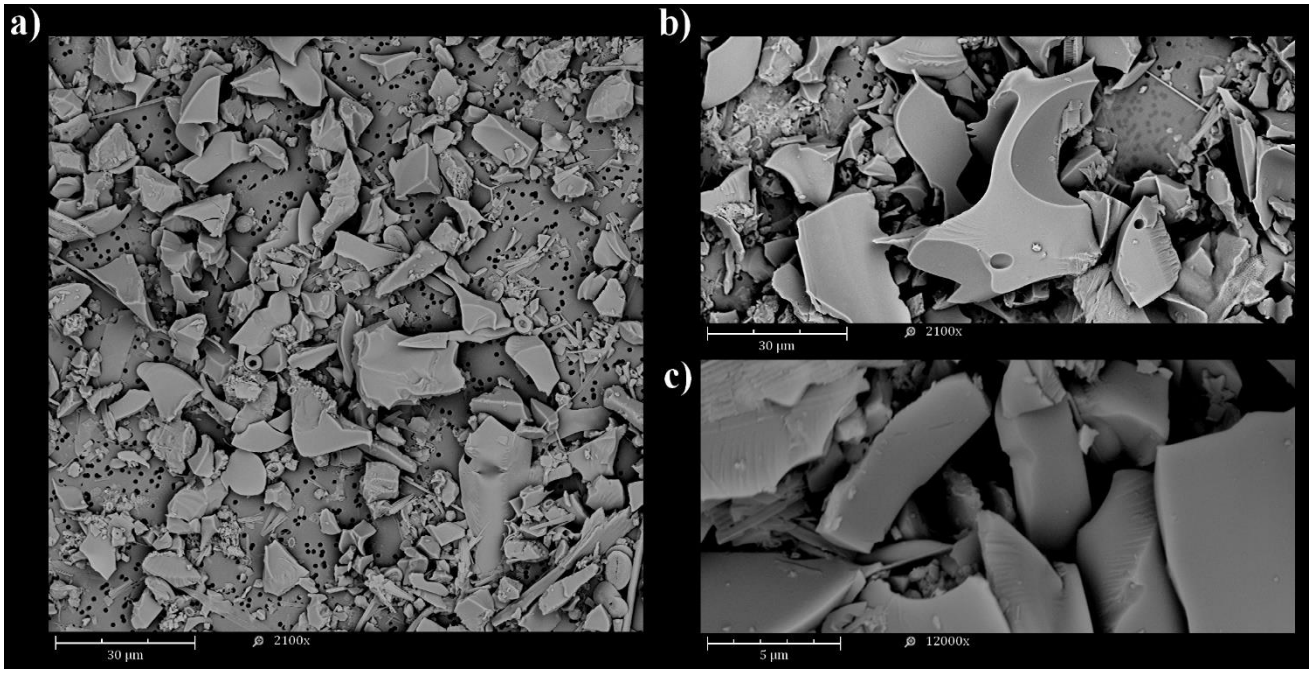

Figure 6. Scanning electron microscopy views of dry material from samples collected in the 1000 m-trap at station 10 where basaltic glass was recovered (magnification **(a, b)**: x2,100 and **(c)**: x12,000).

During the TONGA cruise, a shallow hydrothermal source (~200 m) was identified at station 5. This source was a very active site showing typical acoustic and chemical anomalies such as low pH, low O_2 concentrations and high levels of DFe, DMn, CH_4, CO_2 and H_2S (Tilliette et al., 2022). At 1000 m, the collected particles showed a moderate Boström index (50 ± 1; *Table 3*). This mid-range index probably reflects a mixture of **(1)** hydrothermal material from shallow hydrothermal plumes (~200 m; Tilliette et al., 2022), notably supported by strong Fe_{EF} and Zn_{EF} (*Table 2*, *Fig. 5b*), **(2)** material from the erosion of the New Late'iki volcanic island, according to the westward main current, rich in LSi (LSi_{EF}= 5.2) and Al (*Fig. 5b*) but depleted in Mn (Mn_{EF} = 0.2; *Fig. 5b*) and **(3)** probably some detrital material. In the seafloor sediments, a lower Boström index was estimated (40 ± 2; *Table 3*), possibly due to the additional distal impact from deeper sources (> 1500 m), as Tilliette et al. (2022) measured DFe-rich plume in the deep layer. These sources provided high Fe_{XS} (~5 wt.%), Mn_{XS} (~3 wt.%) and Cu_{XS} (~120 ppm) to these sediments (*Figs. 3, 5c*). The distal hydrothermal origin of the sedimented material was also supported by **(1)** the heterogeneous and large size of particles (> 60 µm), much larger than clays

(< 3 µm; Horn et al., 1970; Leinen, 1989) and typical of distal transport (1-100 µm; Feely et al., 1990, 1987; Lou et al., 2020; Ng et al., 2019), **(2)** the accumulation rates much higher (x116-580) than those of pelagic clays (Li and Schoonmaker, 2003; Piper, 2005) and finally **(3)** the absence of Ni_{XS} and Zn_{XS} throughout the core (*Fig. 3*), these elements being lost near sources. The presence of volcanic material (increasing the index value) is also strongly suspected in the sediments of this station, in view of the continuous LSi_{XS} (up to 5 wt.%; *Fig. 3*) found in the cored sediments at station 5 (dating from the 19th century to the present day according to accumulation rates, see *Table 1*) and the frequent eruptions of the Late'iki volcano since the 18th century (Ewart et al., 1977).

4.4.2 Along the Lau ridge (large scale)

Station 12 was positioned sufficiently far from the identified shallow sources on the Tonga Arc to incorporate their effect on a regional scale. At 200 m, the Boström index was rather high (56 ± 10) but still lower than detrital material (~66; *Table 3*). This signature reflects the likely remote impact of the shallow sources identified along the Tonga Arc (~200 km from station 12), according to the westward main current, supplying low but still significant concentrations of metals within the photic layer, particularly Fe (*Fig. 5a*) in accordance with Fe_{EF} estimated here (*Table 2*). The Boström index variability over the year suggests an important role of subsurface dynamics in delivering lithogenic material at 200 m at station 12. Consistent with this distal contribution, no Cu_{EF} and Ni_{EF} were detected at this trap. As at station 10, a small proportion of the Zn_{EF} can be partially attributed to organic matter supplies (up to 2% biologically-derived Zn, depending on the collection period). At 1000 m, a lower index was measured (43 ± 6; *Table 3*) reflecting an influx of hydrothermal material, especially Fe (Fe_{EF} = 1.7; *Fig. 5b*), from distal shallow or deep source(s) likely located along the Tonga Arc. However, the absence of Mn_{EF} (= 0.6) can be explained through the presence of volcanic material originating from the erosion of the New Late'iki island that brought Al, LSi and Fe-rich but Mn-poor volcanic particles to the trap, thus impacting the measured index (i.e., by increasing it). Indeed, a small LSi_{EF} was visible

during the austral summer period (x3 ± 1 between December 2019 and March 2020), reaching enrichment values up to 7 compared to reference pelagic clays during the period February 8-23, 2020. These LSi_{EF} likely originated from the Late'iki volcano (which erupted in mid-October 2019; Plank et al., 2020) and the subsequent fast erosion of the newly created island (within two months post-eruption), consistent with the main western current potentially carrying basaltic glass to station 12 (Tilliette et al., 2022). This hypothesis is supported by the travel time of particles from station 10 (about 15 km away from New Late'iki) to the fixed trap site at station 12 estimated to be about a hundred days at 1000 m by the Ariane Lagrangian dispersion tool (Grima, pers. comm., 2022; see Section 4.2). Indeed, no further LSi_{EF} was detected at 1000 m at station 12 about 150 days after the submarine volcano eruption (x0.4 ± 0.3 between March and October 2020), and about 70 days after the island disappearance due to erosion, in agreement with the estimated dispersal times at 1000 m. As explained in section 4.3.4, a significant amount of organic material, likely due to fertilization of biological communities through shallow hydrothermal inputs, was collected in the traps deployed at all stations of the Lau Basin. In view of the large quantity of material ejected following the Late'iki eruption, it is interesting to consider possible co-fertilization by both hydrothermal and volcanic processes. However, such volcanic fertilization is unlikely since no volcanic signature was detected in the traps deployed at 200 m and recent studies in the region have demonstrated that volcanic material, particularly basaltic glass, is poorly bioavailable and did not generate a significant response from the biology (Whiteside et al., 2023, 2021).

In seafloor sediments, a mean Boström index of 16 ± 1 reflects a strong hydrothermal signature of a likely near-vent field (*Table 3*) with material exhibiting high Fe_{XS} (up to 5 wt.%) and Mn_{XS} (up to 20 wt.%; *Figs. 3, 5c*). Although this result was unexpected, the presence of a nearby source at the seafloor of station 12 is supported by the high accumulation rates (x122-610 relative to pelagic clays; Li and Schoonmaker, 2003), the particle size distribution, with grain up to 976 µm, typical of near-vent debris

(Feely et al., 1990, 1987; Lou et al., 2020; Ng et al., 2019) as well as the high Zn_{XS}, Ni_{XS} and Cu_{XS} (up to 26, 113 and 259 ppm, respectively). Additional arguments for the presence of strong hydrothermal activity in the vicinity of this station would be **(1)** the numerous reports of discolored waters and volcanic activity according to nautical charts of this area (SHOM C, 6817, INT605), **(2)** many potential active volcanic structures (> 1000 m; GEBCO Bathymetric Compilation Group, 2022), and **(3)** a mega-plume hypothesized within few kilometers of the station (20°28' S, 178°31' W), near the Lau Ridge (Guieu et al., 2018). No LSi_{EF} was estimated in these sediments, revealing that the large particle sizes estimated in this study originate solely from hydrothermal processes, consistent with the high Mn and low Al content.

4.4.3 In the South Pacific gyre

Station 8 is located east of the Tonga Arc and was initially cored as a deep-sea detrital reference. However, its index reveals seafloor sediments displaying a distal field signature, as evidenced by high Fe_{XS} (up to 3 wt.%), Mn_{XS} (up to 6 wt.%), Cu_{XS} (up to 138 ppm) and, to a lesser extent, Pb_{XS} (up to 10 ppm; *Figs 3, 5*) although the estimated elemental excess were lower than in the Lau Basin (up to 5 wt.%, 20 wt.%, 258 ppm and 23 ppm, respectively). Consistent with these observations, the estimated sedimentation rates were 116-580 times higher than those of pelagic sediments (Li and Schoonmaker, 2003; Piper, 2005), indicating a great material flux. It is possible that this material originated from the east, for example from the East Pacific Rise and/or other nearby deep hydrothermal source(s), although no DFe anomalies were detected in the deep waters at this station relative to DFe concentrations in water masses feeding the gyre region, albeit possibly due to the high threshold defined in that study (= 0.2 nmol L^{-1}; Tilliette et al., 2022). This hypothesis is supported by the particle size, which averaged 8 µm, falling within the range of hydrothermal particles involved in long-distance transport (1-50 µm; Feely et al., 1990, 1987; Lou et al., 2020). In addition, hydrothermal plumes have been reported to be transported thousands of kilometers away from their source at the ridge axis (Resing et al., 2015) and

results in continuous fallout of metals over large distances (Lilley et al., 2013), possibly up to station 8. Boström et al. (1969) also demonstrated the presence of sediments influenced by distal hydrothermalism near this site.

4.4.4 Detrital component

As described in section 4.4.1, microscopic inspection of particles collected at selected sediment traps, whether at 200 m or 1000 m, reveals the occurrence of a huge abundance of basaltic glass as evidenced by the sharp angle of large size particles. Escrig et al. (2012) collected fresh volcanic glass along the latitudinal location of the Fonualei Spreading Center (between -18° and -16°S) corresponding to an end-member of global back-arc lavas in the Lau Basin. These volcanic glasses exhibit average (Fe/Mn) ratio and Si content of 54 ± 5 and 25 ± 1 wt.%, respectively. Here, we were able to determine the geochemical composition of the detrital material based on geochemical features measured in the seafloor sediments. Following the calculations presented in section 3.2, the average detrital fraction is characterized by $(Fe/Mn)_{det}$ and Si_{det} at 54 ± 3 and 22 ± 5 wt.%, respectively. These chemical signatures are extremely similar to those of volcanic glasses analyzed by Escrig et al. (2012) as well as for trace metal such as Ni. Nevertheless, the detrital fraction is 10 and 2 times more enriched in Pb and Zn, respectively, which may suggest that the hydrothermal contribution has been underestimated, as mentioned above. Overall, the detrital fraction identified, observed and analyzed here exhibits morphology and geochemical features that are consistent with a nearby volcanic origin solely.

5 Conclusion

In this study, deployment of sediment traps and coring of seafloor sediments allowed the identification and characterization of biogenic and hydrothermally-derived particles along the Tonga Arc over large spatio-temporal scales, from the Lau Ridge to the western border of the South Pacific gyre (along ~20 °S; *Fig. 7*). Consistent with the high biological productivity previously reported in the Lau Basin, large quantities of biogenic material (organic matter, opal and calcium carbonate) were collected at 200 and

1000 m. These particles were intimately related to the influx of lithogenic material from the Tonga Arc, whose hydrothermal origin could be resolved through numerous geochemical tracers (Al, Ca, Cu, Fe, Mn, Ni, Pb, Si, Zn). Such a result suggests that surface production is tightly linked to hydrothermal supply within the Lau Basin photic layer. Seafloor sediments from all stations also exhibited a metal-rich hydrothermal signature (Fe, Mn-rich, Al-depleted), supported by their high accumulation rates as well as the coarse and heterogeneous size of the sedimented particles, typical of hydrothermal oxide and/or sulfide debris. Thus, the sinking and sedimented particles were primarily from shallow to deep hydrothermal sources identified along the Tonga Arc. This set of evidence supports a major influence of hydrothermal sources and refutes the island effect often considered in this region.

Shallow and/or deep hydrothermal sources impacted the composition of sinking and sedimented particles at all stations sampled in the Lau Basin. The effect of the sources on the particle signature depended on their distance from the sampled site. The signature of hydrothermal material was pronounced in the sediment traps deployed at stations 5 and 10 (~15 km from the arc and identified shallow sources). It was also revealed but to a lesser extent at station 12, located near the Lau Ridge (~200 km from the arc), and was primarily reflected through Fe enrichments in the water column both at the surface (200 m) and at depth (1000 m). At all stations, besides the impact of hydrothermalism, a volcanic signature (Fe, LSi, Al-rich, Mn-depleted) was identified in the particles collected in the deepest sediment trap. This abundant volcanic material probably originated from the recent eruption of the Late'iki submarine volcano and the subsequent fast erosion of the newly created island, as confirmed through the observation of basaltic glass in the 1000 m-trap at station 10. Surprisingly, the seafloor at station 12 reflects a deep hydrothermal activity, as evidenced by the typical signature of sulfide debris found near hydrothermal vents and the large and heterogeneous particle size. At the South Pacific gyre deep-sea reference site, the Al-Fe-Mn tracing in the seafloor sediments detected the distal impact of a deep hydrothermal source, likely present along the East Pacific Rise.

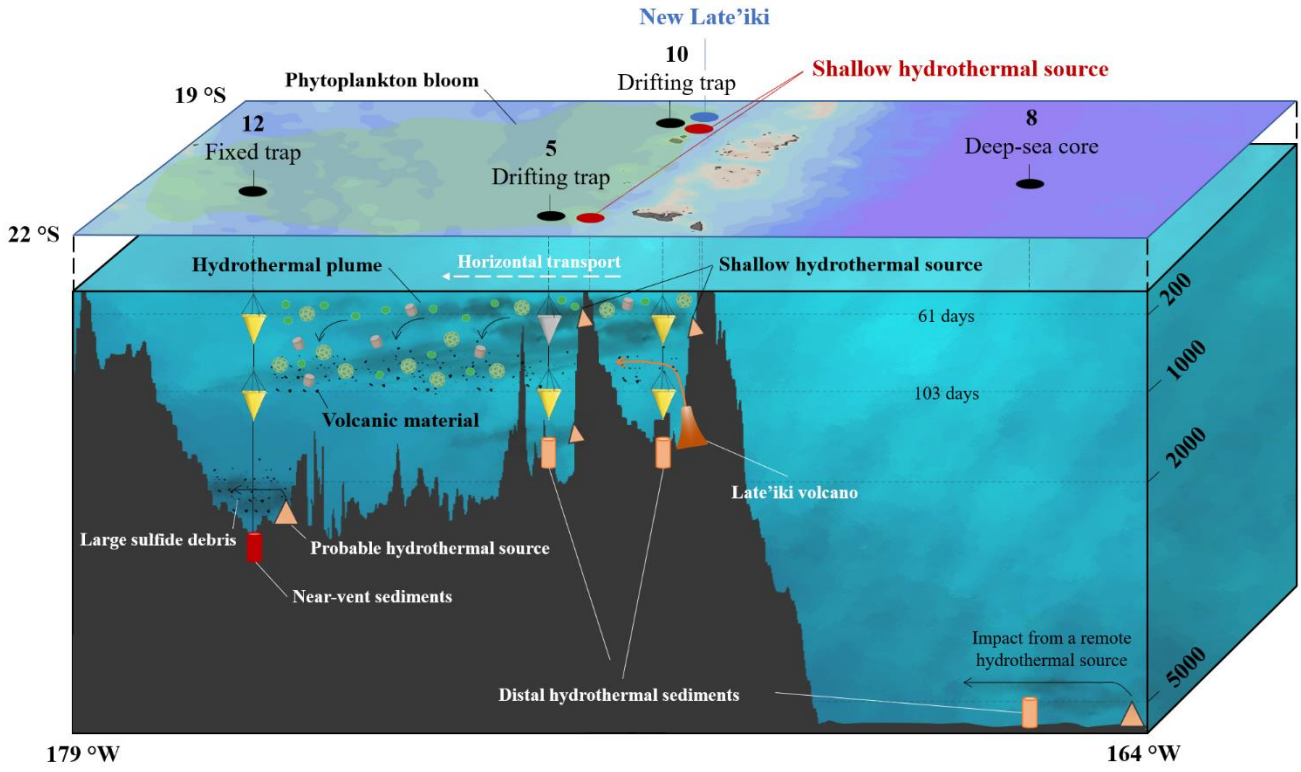

Figure 7. Summary diagram of the main results of the present study. These include **(1)** the non-vertical sinking of particles as well as the greater contribution of material to deep traps due to the longer integration times at depth (specified on the right side of the diagram); **(2)** the impact of shallow hydrothermal plumes on all sediment traps in the Lau Basin; **(3)** the impact of volcanic material from the Late'iki volcano eruption on the deep traps deployed at stations 5, 10 and 12; **(4)** the impact of shallow and deep hydrothermalism, along with submarine volcanism, on seafloor sediments; **(5)** the impact of a distal hydrothermal source on the sediments at the deep-sea reference site; and **(6)** the impact of the potential deep hydrothermal source deduced near station 12. Note that no sample could be collected from the 200 m-trap deployed at station 5 (shaded) due to a PPS-5 malfunction. The days shown on the 200 and 1000 m lines indicate the travel time of particles from the Tonga Arc to the fixed trap site at these depths.

All these data lead to the conclusion that a myriad of shallow and deep hydrothermal sources, located along the Tonga Arc, fertilize the entire Lau Basin with numerous elements, including Fe, triggering significant POC production. These hydrothermal sources, along with submarine volcanism, have a significant impact on the biogeochemistry of the Lau Basin, at very large spatial (from the Tonga Arc to the Lau Ridge) and temporal (from seasonal to centennial time scales in seafloor sediments) scales.

This study also illustrates the importance of employing considerable care in interpreting sediment trap data, as these are certainly influenced by physical dynamics, thus greatly affecting the vertical sinking of collected particles.

Future research is needed to probe the seafloor near station 12 for acoustic and chemical anomalies to identify the hydrothermal source(s) responsible for the presence of large, metal-rich sedimented particles. Finally, molecular analyses could be interesting to characterize the different bacteria and/or archaea present in the water-sediment interface and to draw conclusions on the low $CaCO_3$ preservation observed in the seafloor sediments along the Tonga Arc.

6 Declaration of Competing Interest

The authors declare that they have no known competing financial interests or personal relationships that could have appeared to influence the work reported in this paper.

7 Acknowledgments

This work was carried out in the framework of the TONGA project (TONGA cruise GEOTRACES GPpr14, November 2019, https://doi.org/10.17600/18000884) managed by the LOV (CG) and the MIO. The project was funded by the TGIR Flotte Océanographique Française, the A-MIDeX of Aix-Marseille University, the LEFE-CYBER and GMMC program and the Agence Nationale de Recherche (ANR-18-CE01-0016). We warmly thank all the scientists, the captain and the crew of the R/V L'Atalante for their cooperative work at sea. We thank Faustine Fauche for her help in the analysis of trap and core samples. We thank Céline Dimier and the SAPIGH platform for the pigment analyzes as well as the SNAPO-CO_2 platform for carbonate chemistry analyzes. We thank Christophe Maes and Nicolas Grima for their help in positioning the fixed mooring line and for the Lagrangian analyses.

8 Supplementary Material

Supplementary material to this article is the following: Supplementary information 1 (PDF file)

9 Data availability

All the data used in this study will be accessible as soon as they are published on the SEANOE database (https://www.seanoe.org/data/00770/88169/) and on the LEFE-CYBER database (http://www.obs-vlfr.fr/proof/php/TONGA/tonga.php).

10 References

Almirón, J., Vargas, M., Tupayachy-Quispe, D., Duquesne, S., Roudet, F., Silva-Vela, A., 2021. Influence of the Process of Synthesis of Zeolites from Volcanic Ash in Its Synergistic Action as a Flame-Retardant for Polypropylene Composites. Buildings 12, 24. https://doi.org/10.3390/buildings12010024

Anderson, M.O., Norris-Julseth, C., Rubin, K.H., Haase, K., Hannington, M.D., Baxter, A.T., Stewart, M.S., 2021. Geologic and Structural Evolution of the NE Lau Basin, Tonga: Morphotectonic Analysis and Classification of Structures Using Shallow Seismicity. Front. Earth Sci. 9, 665185. https://doi.org/10.3389/feart.2021.665185

Bailey, D.K., 1993. Carbonate magmas. JGS 150, 637–651. https://doi.org/10.1144/gsjgs.150.4.0637

Baker, C.A., Estapa, M.L., Iversen, M., Lampitt, R., Buesseler, K., 2020. Are all sediment traps created equal? An intercomparison study of carbon export methodologies at the PAP-SO site. Progress in Oceanography 184, 102317. https://doi.org/10.1016/j.pocean.2020.102317

Baker, E.T., Walker, S.L., Massoth, G.J., Resing, J.A., 2019. The NE Lau Basin: Widespread and Abundant Hydrothermal Venting in the Back-Arc Region Behind a Superfast Subduction Zone. Front. Mar. Sci. 6, 382. https://doi.org/10.3389/fmars.2019.00382

Barrett, T.J., Jarvis, I., Hannington, M.D., Thirlwall, M.F., 2021. Chemical characteristics of modern deep-sea metalliferous sediments in closed versus open basins, with emphasis on rare-earth elements and Nd isotopes. Earth-Science Reviews 222, 103801. https://doi.org/10.1016/j.earscirev.2021.103801

Beaulieu, S.E., Szafrański, K.M., 2020. InterRidge Global Database of Active Submarine Hydrothermal Vent Fields Version 3.4. https://doi.org/10.1594/PANGAEA.917894

Berger, W.H., Smetacek, V., Wefer, G., 1989. Ocean productivity and paleoproductivity - an overview, in: Productivity of the Oceans Present and Past. Wiley, Berlin, pp. 1–34.

Bodungen, B.V., Wunsch, M., Fürderer, H., 2013. Sampling and Analysis of Suspended and Sinking Particles in the Northern North Atlantic, in: Hurd, D.C., Spencer, D.W. (Eds.), Geophysical Monograph Series. American Geophysical Union, Washington, D. C., pp. 47–56. https://doi.org/10.1029/GM063p0047

Bonnet, S., Caffin, M., Berthelot, H., Moutin, T., 2017. Hot spot of N_2 fixation in the western tropical South Pacific pleads for a spatial decoupling between N_2 fixation and denitrification. Proc Natl Acad Sci USA 114, E2800–E2801. https://doi.org/10.1073/pnas.1619514114

Bonnet, S., Guieu, C., Taillandier, V., Boulart, C., Bouruet-Aubertot, P., Gazeau, F., Bressac, M., Knapp, A.N., Cuypers, Y., González-Santana, D., Forrer, H.J., Grisoni, J.-M., Grosso, O., Habasque, J., Jardin-Camps, M., Leblond, N., Le Moigne, F., Lebourges-Dhaussy, A., Lory,

C., Nunige, S., Pulido-Villena, E., Rizzo, A.L., Sarthou, G., Tilliette, C., in rev. Natural iron fertilization by shallow hydrothermal sources fuels diazotroph blooms in the Ocean. Science.

Boström, K., Peterson, M.N.A., 1969. The origin of aluminum-poor ferromanganoan sediments in areas of high heat flow on the East Pacific Rise. Marine Geology 7, 427–447. https://doi.org/10.1016/0025-3227(69)90016-4

Boström, K., Peterson, M.N.A., Joensuu, O., Fisher, D.E., 1969. Aluminum-poor ferromanganoan sediments on active oceanic ridges. J. Geophys. Res. 74, 3261–3270. https://doi.org/10.1029/JB074i012p03261

Boyd, P.W., Trull, T.W., 2007. Understanding the export of biogenic particles in oceanic waters: Is there consensus? Progress in Oceanography 72, 276–312. https://doi.org/10.1016/j.pocean.2006.10.007

Brzezinski, M.A., Nelson, D.M., 1995. The annual silica cycle in the Sargasso Sea near Bermuda. Deep Sea Research Part I: Oceanographic Research Papers 42, 1215–1237. https://doi.org/10.1016/0967-0637(95)93592-3

Buesseler, K.O., Antia, A.N., Chen, M., Fowler, S.W., Gardner, W.D., Gustafsson, O., Harada, K., Michaels, A.F., Rutgers van der Loeff, M., Sarin, M., Steinberg, D.K., Trull, T., 2007. An assessment of the use of sediment traps for estimating upper ocean particle fluxes. j mar res 65, 345–416. https://doi.org/10.1357/002224007781567621

Butman, C.A., 1986. Sediment trap biases in turbulent flows: Results from a laboratory flume study. Journal of Marine Research 44, 645–693. https://doi.org/10.1357/002224086788403051

Carpenter, E.J., Capone, D.G., 1992. Nitrogen Fixation in Trichodesmium Blooms, in: Carpenter, E. J., Capone, D. G., Rueter, J.G. (Eds.), Marine Pelagic Cyanobacteria: Trichodesmium and Other Diazotrophs, NATO ASI Series. Springer Netherlands, Dordrecht, pp. 211–217. https://doi.org/10.1007/978-94-015-7977-3_13

Cave, R., 2002. A Geochemical Study of Hydrothermal Signals in Marine Sediments: The Rainbow Hydro thermal Area, 36 degrees on the Mid-Atlantic Ridge (PhD Thesis). University of Southampton.

Cave, R.R., German, C.R., Thomson, J., Nesbitt, R.W., 2002. Fluxes to sediments underlying the Rainbow hydrothermal plume at 36°14′N on the Mid-Atlantic Ridge. Geochimica et Cosmochimica Acta 66, 1905–1923. https://doi.org/10.1016/S0016-7037(02)00823-2

Chavagnac, V., German, C.R., Milton, J.A., Palmer, M.R., 2005. Sources of REE in sediment cores from the Rainbow vent site (36°14′N, MAR). Chemical Geology 216, 329–352. https://doi.org/10.1016/j.chemgeo.2004.11.015

Chavagnac, V., German, C.R., Taylor, R.N., 2008. Global environmental effects of large volcanic eruptions on ocean chemistry: Evidence from “hydrothermal” sediments (ODP Leg 185, Site 1149B). J. Geophys. Res. 113, B06201. https://doi.org/10.1029/2007JB005333

Cronan, D.S., 1972. The Mid-Atlantic Ridge near 45 °N, XVII: Al, As, Hg, and Mn in Ferruginous Sediments from the Median Valley. Can. J. Earth Sci. 9, 319–323. https://doi.org/10.1139/e72-025

Deuser, W.G., 1987. Seasonal variations in isotopic composition and deep-water fluxes of the tests of perennially abundant planktonic foraminifera of the Sargasso Sea; results from sediment-trap collections and their paleoceanographic significance. The Journal of Foraminiferal Research 17, 14–27. https://doi.org/10.2113/gsjfr.17.1.14

Deuser, W.G., Ross, E.H., 1980. Seasonal change in the flux of organic carbon to the deep Sargasso Sea. Nature 283, 364–365. https://doi.org/10.1038/283364a0

Dick, G.J., Anantharaman, K., Baker, B.J., Li, M., Reed, D.C., Sheik, C.S., 2013. The microbiology of deep-sea hydrothermal vent plumes: ecological and biogeographic linkages to seafloor and water column habitats. Front. Microbiol. 4. https://doi.org/10.3389/fmicb.2013.00124

Ducklow, H., Steinberg, D., Buesseler, K., 2001. Upper Ocean Carbon Export and the Biological Pump. oceanog 14, 50–58. https://doi.org/10.5670/oceanog.2001.06

Dutkiewicz, A., Müller, R.D., Hogg, A.McC., Spence, P., 2016. Vigorous deep-sea currents cause global anomaly in sediment accumulation in the Southern Ocean. Geology 44, 663–666. https://doi.org/10.1130/G38143.1

Dymond, J., 1981. Geochemistry of Nazca plate surface sediments: An evaluation of hydrothermal, biogenic, detrital, and hydrogenous sources, in: Geological Society of America Memoirs. Geological Society of America, pp. 133–174. https://doi.org/10.1130/MEM154-p133

Edmonds, H.N., German, C.R., 2004. Particle geochemistry in the Rainbow hydrothermal plume, Mid-Atlantic Ridge. Geochimica et Cosmochimica Acta 68, 759–772. https://doi.org/10.1016/S0016-7037(03)00498-8

Emerson, S., Hedges, J.I., 1988. Processes controlling the organic carbon content of open ocean sediments. Paleoceanography 3, 621–634. https://doi.org/10.1029/PA003i005p00621

Escrig, S., Bézos, A., Langmuir, C.H., Michael, P.J., Arculus, R., 2012. Characterizing the effect of mantle source, subduction input and melting in the Fonualei Spreading Center, Lau Basin: Constraints on the origin of the boninitic signature of the back-arc lavas: GEOCHEMICAL VARIATION ALONG THE FSC. Geochem. Geophys. Geosyst. 13, n/a-n/a. https://doi.org/10.1029/2012GC004130

Ewart, A., Brothers, R.N., Mateen, A., 1977. An outline of the geology and geochemistry, and the possible petrogenetic evolution of the volcanic rocks of the Tonga-Kermadec-New Zealand island arc. Journal of Volcanology and Geothermal Research 2, 205–250. https://doi.org/10.1016/0377-0273(77)90001-4

Feely, R.A., Geiselman, T.L., Baker, E.T., Massoth, G.J., Hammond, S.R., 1990. Distribution and composition of hydrothermal plume particles from the ASHES Vent Field at Axial Volcano, Juan de Fuca Ridge. J. Geophys. Res. 95, 12855. https://doi.org/10.1029/JB095iB08p12855

Feely, R.A., Lewison, M., Massoth, G.J., Robert-Baldo, G., Lavelle, J.W., Byrne, R.H., Von Damm, K.L., Curl, H.C., 1987. Composition and dissolution of black smoker particulates from active vents on the Juan de Fuca Ridge. J. Geophys. Res. 92, 11347–11363. https://doi.org/10.1029/JB092iB11p11347

Fiantis, D., Nelson, M., Shamshuddin, J., Goh, T.B., Van Ranst, E., 2010. Determination of the geochemical weathering indices and trace elements content of new volcanic ash deposits from Mt. Talang (West Sumatra) Indonesia. Eurasian Soil Sc. 43, 1477–1485. https://doi.org/10.1134/S1064229310130077

Gardner, W., 1980. Field calibration of sediment traps. Journal of Marine Research 30, 311–323.

GEBCO Bathymetric Compilation Group 2022, 2022. The GEBCO_2022 Grid - a continuous terrain model of the global oceans and land. https://doi.org/10.5285/E0F0BB80-AB44-2739-E053-6C86ABC0289C

German, C.R., Bourlés, D.L., Brown, E.T., Hergt, J., Colley, S., Higgs, N.C., Ludford, E.M., Nelsen, T.A., Feely, R.A., Raisbeck, G., Yiou, F., 1997. Hydrothermal scavenging on the Juan de Fuca Ridge: 23OThxs, 10Be, and REEs in ridge-flank sediments. Geochimica et Cosmochimica Acta 61, 4067–4078. https://doi.org/10.1016/S0016-7037(97)00230-5

Gersonde, R., Crosta, X., Abelmann, A., Armand, L., 2005. Sea-surface temperature and sea ice distribution of the Southern Ocean at the EPILOG Last Glacial Maximum—a circum-Antarctic view based on siliceous microfossil records. Quaternary Science Reviews 24, 869–896. https://doi.org/10.1016/j.quascirev.2004.07.015

González-Vega, A., Fraile-Nuez, E., Santana-Casiano, J.M., González-Dávila, M., Escánez-Pérez, J., Gómez-Ballesteros, M., Tello, O., Arrieta, J.M., 2020. Significant Release of Dissolved Inorganic Nutrients From the Shallow Submarine Volcano Tagoro (Canary Islands) Based on Seven-Year Monitoring. Front. Mar. Sci. 6, 829. https://doi.org/10.3389/fmars.2019.00829

Guieu, C., Bonnet, S., 2019. TONGA cruise 2019, L'Atalante R/V. https://doi.org/10.17600/18000884

Guieu, C., Bonnet, S., Petrenko, A., Menkes, C., Chavagnac, V., Desboeufs, K., Maes, C., Moutin, T., 2018. Iron from a submarine source impacts the productive layer of the Western Tropical South Pacific (WTSP). Sci Rep 8, 1–9. https://doi.org/10.1038/s41598-018-27407-z

Hargrave, B.T., Burns, N.M., 1979. Assessment of sediment trap collection efficiency. Limnol. Oceanogr. 24, 1124–1136. https://doi.org/10.4319/lo.1979.24.6.1124

Ho, T.-Y., Quigg, A., Finkel, Z.V., Milligan, A.J., Wyman, K., Falkowski, P.G., Morel, F.M.M., 2003. The Elemental Composition of Some Marine Phytoplankton. Journal of Phycology 39, 1145–1159. https://doi.org/10.1111/j.0022-3646.2003.03-090.x

Honjo, S., Spencer, D.W., Gardner, W.D., 1992. A sediment trap intercomparison experiment in the Panama Basin, 1979. Deep Sea Research Part A. Oceanographic Research Papers 39, 333–358. https://doi.org/10.1016/0198-0149(92)90112-7

Horn, D.R., Horn, B.M., Delach, M.N., 1970. Sedimentary Provinces of the North Pacific, in: Geological Society of America Memoirs. Geological Society of America, pp. 1–22. https://doi.org/10.1130/MEM126-p1

Humphris, S.E., Herzig, P.M., Miller, D.J., Alt, J.C., Becker, K., Brown, D., Brügmann, G., Chiba, H., Fouquet, Y., Gemmell, J.B., Guerin, G., Hannington, M.D., Holm, N.G., Honnorez, J.J., Iturrino, G.J., Knott, R., Ludwig, R., Nakamura, K., Petersen, S., Reysenbach, A.-L., Rona, P.A., Smith, S., Sturz, A.A., Tivey, M.K., Zhao, X., 1995. The internal structure of an active sea-floor massive sulphide deposit. Nature 377, 713–716. https://doi.org/10.1038/377713a0

Hüneke, H., Henrich, R., 2011. Pelagic Sedimentation in Modern and Ancient Oceans, in: Developments in Sedimentology. Elsevier, pp. 215–351. https://doi.org/10.1016/B978-0-444-53000-4.00004-4

Hurd, D.C., 1972. Factors affecting solution rate of biogenic opal in seawater. Earth and Planetary Science Letters 15, 411–417. https://doi.org/10.1016/0012-821X(72)90040-4

Imai, N., Terashima, S., Itoh, S., Ando, A., 1995. 1994 Compilation of analytical data for minor and trace elements in seventeen GSJ geochemical reference samples, "igneous rock series." Geostandards and Geoanalytical Research 19, 135–213. https://doi.org/10.1111/j.1751-908X.1995.tb00158.x

Karl, D.M., 1995. The microbiology of deep-sea hydrothermal vents, CRC-Press. ed.

Klaas, C., Archer, D.E., 2002. Association of sinking organic matter with various types of mineral ballast in the deep sea: Implications for the rain ratio. Global Biogeochem. Cycles 16, 63-1-63–14. https://doi.org/10.1029/2001GB001765

Kyte, F.T., Leinen, M., Ross Heath, G., Zhou, L., 1993. Cenozoic sedimentation history of the central North Pacific: Inferences from the elemental geochemistry of core LL44-GPC3. Geochimica et Cosmochimica Acta 57, 1719–1740. https://doi.org/10.1016/0016-7037(93)90109-A

Leinen, M., 1989. The pelagic clay province of the North Pacific Ocean, in: Winterer, E.L., Hussong, D.M., Decker, R.W. (Eds.), The Eastern Pacific Ocean and Hawaii. Geological Society of America, North America, pp. 323–335. https://doi.org/10.1130/DNAG-GNA-N.323

Leonelli, C., Kamseu, E., Boccaccini, D.N., Melo, U.C., Rizzuti, A., Billong, N., Miselli, P., 2007. Volcanic ash as alternative raw materials for traditional vitrified ceramic products. Advances in Applied Ceramics 106, 135–141. https://doi.org/10.1179/174367607X159329

Li, Y.-H., Schoonmaker, J.E., 2003. Chemical Composition and Mineralogy of Marine Sediments, in: Treatise on Geochemistry. Elsevier, pp. 1–35. https://doi.org/10.1016/B0-08-043751-6/07088-2

Lilley, M.D., Feely, R.A., Trefry, J.H., 2013. Chemical and Biochemical Transformations in Hydrothermal Plumes, in: Seafloor Hydrothermal Systems: Physical, Chemical, Biological, and Geological Interactions. American Geophysical Union (AGU), pp. 369–391. https://doi.org/10.1029/GM091p0369

Locarnini, R., Mishonov, A., Baranova, O., Boyer, T., Zweng, M., Garcia, H., Reagan, J., Seidov, D., Weathers, K., Paver, C., 2018. World Ocean Atlas 2018, Volume 1: Temperature. NOAA Atlas NESDIS 81 52.

Lou, Y., He, Z., Han, X., 2020. Transport and Deposition Patterns of Particles Laden by Rising Submarine Hydrothermal Plumes. Geophys. Res. Lett. 47. https://doi.org/10.1029/2020GL089935

Lupton, J.E., Pyle, D.G., Jenkins, W.J., Greene, R., Evans, L., 2004. Evidence for an extensive hydrothermal plume in the Tonga-Fiji region of the South Pacific. Geochem. Geophys. Geosyst. 5. https://doi.org/10.1029/2003GC000607

Mahiques, M.M., Sousa, S.H.M., Burone, L., Nagai, R.H., Silveira, I.C.A., Figueira, R.C.L., Soutelino, R.G., Ponsoni, L., Klein, D.A., 2011. Radiocarbon geochronology of the sediments of the São Paulo Bight (southern Brazilian upper margin). An. Acad. Bras. Ciênc. 83, 817–834. https://doi.org/10.1590/S0001-37652011005000028

Massoth, G., Baker, E., Worthington, T., Lupton, J., de Ronde, C., Arculus, R., Walker, S., Nakamura, K., Ishibashi, J., Stoffers, P., Resing, J., Greene, R., Lebon, G., 2007. Multiple hydrothermal sources along the south Tonga arc and Valu Fa Ridge. Geochem. Geophys. Geosyst. 8. https://doi.org/10.1029/2007GC001675

Massoth, G.J., Baker, E.T., Feely, R.A., Lupton, J.E., Collier, R.W., Gendron, J.F., Roe, K.K., Maenner, S.M., Resing, J.A., 1998. Manganese and iron in hydrothermal plumes resulting from the 1996 Gorda Ridge Event. Deep Sea Research Part II: Topical Studies in Oceanography 45, 2683–2712. https://doi.org/10.1016/S0967-0645(98)00089-7

Mills, R., Elderfield, H., Thomson, J., 1993. A dual origin for the hydrothermal component in a metalliferous sediment core from the Mid-Atlantic Ridge. J. Geophys. Res. 98, 9671. https://doi.org/10.1029/92JB01414

Mills, R.A., Elderfield, H., 1995. Hydrothermal Activity and the Geochemistry of Metalliferous Sediment, in: Humphris, S.E., Zierenberg, R.A., Mullineaux, L.S., Thomson, R.E. (Eds.), Geophysical Monograph Series. American Geophysical Union, Washington, D. C., pp. 392–407. https://doi.org/10.1029/GM091p0392

Morse, J.W., Arvidson, R.S., Lüttge, A., 2007. Calcium Carbonate Formation and Dissolution. Chem. Rev. 107, 342–381. https://doi.org/10.1021/cr050358j

Mortlock, R.A., Froelich, P.N., 1989. A simple method for the rapid determination of biogenic opal in pelagic marine sediments. Deep Sea Research Part A. Oceanographic Research Papers 36, 1415–1426. https://doi.org/10.1016/0198-0149(89)90092-7

Mosseri, J., Quéguiner, B., Rimmelin, P., Leblond, N., Guieu, C., 2005. Silica fluxes in the northeast Atlantic frontal zone of Mode Water formation (38°–45°N, 16°–22°W) in 2001–2002. J. Geophys. Res. 110, C07S19. https://doi.org/10.1029/2004JC002615

Naji, J.A., Asi, I.M., 2008. Performance Evaluation of Asphalt Concrete Mixes Containing Granular Volcanic Ash. J. Mater. Civ. Eng. 20, 754–761. https://doi.org/10.1061/(ASCE)0899-1561(2008)20:12(754)

Nelson, D.M., Brzezinski, M.A., 1997. Diatom growth and productivity in an oligo-trophic midocean gyre: A 3-yr record from the Sargasso Sea near Bermuda. Limnol. Oceanogr. 42, 473–486. https://doi.org/10.4319/lo.1997.42.3.0473

Nelson, D.M., Smith, W.O., Muench, R.D., Gordon, L.I., Sullivan, C.W., Husby, D.M., 1989. Particulate matter and nutrient distributions in the ice-edge zone of the Weddell Sea: relationship to hydrography during late summer. Deep Sea Research Part A. Oceanographic Research Papers 36, 191–209. https://doi.org/10.1016/0198-0149(89)90133-7

Nelson, D.M., Tréguer, P., Brzezinski, M.A., Leynaert, A., Quéguiner, B., 1995. Production and dissolution of biogenic silica in the ocean: Revised global estimates, comparison with regional data and relationship to biogenic sedimentation. Global Biogeochemical Cycles 9, 359–372. https://doi.org/10.1029/95GB01070

Ng, W.-L., Chen, C.-A., Kawi, S.D., Musta, B., Chan, T.-Y., 2019. Effects of hydrogen peroxide treatment on the particle size distribution of hydrothermal vent sediments: A case study in Guishan Island, Taiwan. Borneo Journal of Marine Science and Aquaculture (BJoMSA) 3, 52–56. https://doi.org/10.51200/bjomsa.v3i2.1995

Nohara, M., Yokoto, S., 1978. The Geochemistry of Trace Elements in Pelagic Sediments from the Central Pacific Basin. The Journal of the Geological Society of Japan 84. https://doi.org/10.5575/geosoc.84.165

Oskarasson, N., 2010. Chemical analysis of rocks from the Eyjafjallajökull 2010 eruptions.

Owens, S., Buesseler, K.O., Lamborg, C.H., Valdes, J.R., Lomas, L., Johnson, R., Steinberg, D., Siegel, D.A., 2013. A new time series of particle export from neutrally buoyant sediments traps at the Bermuda Atlantic Time-series Study site. Deep Sea Research Part I: Oceanographic Research Papers 72, 34–47. https://doi.org/10.1016/j.dsr.2012.10.011

Pelletier, B., Calmant, S., Pillet, R., 1998. Current tectonics of the Tonga–New Hebrides region. Earth and Planetary Science Letters 164, 263–276. https://doi.org/10.1016/S0012-821X(98)00212-X

Piper, D.J.W., 2005. SEDIMENTARY PROCESSES | Deep Water Processes and Deposits, in: Encyclopedia of Geology. Elsevier, pp. 641–649. https://doi.org/10.1016/B0-12-369396-9/00496-2

938 Plank, S., Marchese, F., Genzano, N., Nolde, M., Martinis, S., 2020. The short life of the volcanic
939 island New Late'iki (Tonga) analyzed by multi-sensor remote sensing data. Sci Rep 10, 22293.
940 https://doi.org/10.1038/s41598-020-79261-7

941 Plank, T., Kelley, K.A., Murray, R.W., Stern, L.Q., 2007. Chemical composition of sediments
942 subducting at the Izu-Bonin trench: CHEMICAL COMPOSITION OF SEDIMENTS.
943 Geochem. Geophys. Geosyst. 8, n/a-n/a. https://doi.org/10.1029/2006GC001444

944 Raven, J.A., 1988. The iron and molybdenum use efficiencies of plant growth with different energy,
945 carbon and nitrogen sources. New Phytol 109, 279–287. https://doi.org/10.1111/j.1469-
946 8137.1988.tb04196.x

947 Razzhigaeva, N.G., Ganzei, L.A., Grebennikova, T.A., Mokhova, L.M., Kopoteva, T.A., Rybin, A.V.,
948 Kharlamov, A.A., 2009. The peat bog of Ketoi Island: The Middle-Upper Holocene reference
949 section of the Central Kuriles. Russ. J. of Pac. Geol. 3, 570–584.
950 https://doi.org/10.1134/S1819714009060050

951 Redfield, A.C., Ketchum, B.H., Richards, F.A., 1963. The influence of organisms on the composition
952 of sea-water, in: The Composition of Seawater: Comparative and Descriptive Oceanography,
953 The Sea. Interscience Publishers: New York, pp. 26–77.

954 Resing, J.A., Sansone, F.J., 1999. The chemistry of lava–seawater interactions: the generation of
955 acidity. Geochimica et Cosmochimica Acta 63, 2183–2198. https://doi.org/10.1016/S0016-
956 7037(99)00193-3

957 Resing, J.A., Sedwick, P.N., German, C.R., Jenkins, W.J., Moffett, J.W., Sohst, B.M., Tagliabue, A.,
958 2015. Basin-scale transport of hydrothermal dissolved metals across the South Pacific Ocean.
959 Nature 523, 200–203. https://doi.org/10.1038/nature14577

960 Robbins, J.A., Edgington, D.N., 1975. Determination of recent sedimentation rates in Lake Michigan
961 using Pb-210 and Cs-137. Geochimica et Cosmochimica Acta 39, 285–304.
962 https://doi.org/10.1016/0016-7037(75)90198-2

963 Rousselet, L., de Verneil, A., Doglioli, A.M., Petrenko, A.A., Duhamel, S., Maes, C., Blanke, B., 2018.
964 Large- to submesoscale surface circulation and its implications on biogeochemical/biological
965 horizontal distributions during the OUTPACE cruise (southwest Pacific). Biogeosciences 15,
966 2411–2431. https://doi.org/10.5194/bg-15-2411-2018

967 Sarmiento, J.L., Gruber, N., 2006. Ocean biogeochemical dynamics. Princeton University Press,
968 Princeton.

969 Sayles, F.L., Bischoff, J.L., 1973. Ferromanganoan sediments in the equatorial East Pacific. Earth and
970 Planetary Science Letters 19, 330–336. https://doi.org/10.1016/0012-821X(73)90083-6

971 Schmidt, S., Howa, H., Diallo, A., Martín, J., Cremer, M., Duros, P., Fontanier, C., Deflandre, B.,
972 Metzger, E., Mulder, T., 2014. Recent sediment transport and deposition in the Cap-Ferret
973 Canyon, South-East margin of Bay of Biscay. Deep Sea Research Part II: Topical Studies in
974 Oceanography 104, 134–144. https://doi.org/10.1016/j.dsr2.2013.06.004

975 Scholten, J.C., Fietzke, J., Vogler, S., Rutgers van der Loeff, M.M., Mangini, A., Koeve, W., Waniek,
976 J., Stoffers, P., Antia, A., Kuss, J., 2001. Trapping efficiencies of sediment traps from the deep
977 Eastern North Atlantic: Deep Sea Research Part II: Topical Studies in Oceanography 48, 2383–
978 2408. https://doi.org/10.1016/S0967-0645(00)00176-4

979 Stoffers, P., Worthington, T.J., Schwarz-Schampera, U., Hannington, M.D., Massoth, G.J., Hekinian,
980 R., Schmidt, M., Lundsten, L.J., Evans, L.J., Vaiomo'unga, R., Kerby, T., 2006. Submarine

volcanoes and high-temperature hydrothermal venting on the Tonga arc, southwest Pacific. Geol 34, 453. https://doi.org/10.1130/G22227.1

Taylor, S.R., McLennan, S.M., 1985. The continental crust: its composition and evolution: an examination of the geochem. record preserved in sedimentary rocks, Geoscience texts. Blackwell, Oxford.

Tchakoute Kouamo, H., Elimbi, A., Mbey, J.A., Ngally Sabouang, C.J., Njopwouo, D., 2012. The effect of adding alumina-oxide to metakaolin and volcanic ash on geopolymer products: A comparative study. Construction and Building Materials 35, 960–969. https://doi.org/10.1016/j.conbuildmat.2012.04.023

Tilliette, C., Taillandier, V., Bouruet-Aubertot, P., Grima, N., Maes, C., Montanes, M., Sarthou, G., Vorrath, M.-E., Arnone, V., Bressac, M., González-Santana, D., Gazeau, F., Guieu, C., 2022. Dissolved iron patterns impacted by shallow hydrothermal sources along a transect through the Tonga-Kermadec arc. Global Biogeochemical Cycles. https://doi.org/10.1029/2022GB007363

Timm, C., Bassett, D., Graham, I.J., Leybourne, M.I., de Ronde, C.E.J., Woodhead, J., Layton-Matthews, D., Watts, A.B., 2013. Louisville seamount subduction and its implication on mantle flow beneath the central Tonga–Kermadec arc. Nat Commun 4, 1720. https://doi.org/10.1038/ncomms2702

Tréguer, P., Nelson, D.M., Van Bennekom, A.J., DeMaster, D.J., Leynaert, A., Quéguiner, B., 1995. The Silica Balance in the World Ocean: A Reestimate. Science 268, 375–379. https://doi.org/10.1126/science.268.5209.375

Trocine, R.P., Trefry, J.H., 1988. Distribution and chemistry of suspended particles from an active hydrothermal vent site on the Mid-Atlantic Ridge at 26°N. Earth and Planetary Science Letters 88, 1–15. https://doi.org/10.1016/0012-821X(88)90041-6

Turner, J., 2002. Zooplankton fecal pellets, marine snow and sinking phytoplankton blooms. Aquat. Microb. Ecol. 27, 57–102. https://doi.org/10.3354/ame027057

Verardo, D.J., Froelich, P.N., McIntyre, A., 1990. Determination of organic carbon and nitrogen in marine sediments using the Carlo Erba NA-1500 analyzer. Deep Sea Research Part A. Oceanographic Research Papers 37, 157–165. https://doi.org/10.1016/0198-0149(90)90034-S

Volk, T., Hoffert, M.I., 2013. Ocean Carbon Pumps: Analysis of Relative Strengths and Efficiencies in Ocean-Driven Atmospheric CO_2 Changes, in: Sundquist, E.T., Broecker, W.S. (Eds.), Geophysical Monograph Series. American Geophysical Union, Washington, D. C., pp. 99–110. https://doi.org/10.1029/GM032p0099

Von Damm, K.L., 1990. Seafloor hydrothermal activity: black smoker chemistry and chimneys. Annual Review of Earth and Planetary Sciences 18, 173–204.

Wefer, G., Fischer, G., 1993. Seasonal patterns of vertical particle flux in equatorial and coastal upwelling areas of the eastern Atlantic. Deep Sea Research Part I: Oceanographic Research Papers 40, 1613–1645. https://doi.org/10.1016/0967-0637(93)90019-Y

Whiteside, A., Dupouy, C., Singh, A., Bani, P., Tan, J., Frouin, R., 2023. Impact of ashes from the 2022 Tonga volcanic eruption on satellite ocean color signatures. Front. Mar. Sci. 9, 1028022. https://doi.org/10.3389/fmars.2022.1028022

Whiteside, A., Dupouy, C., Singh, A., Frouin, R., Menkes, C., Lefèvre, J., 2021. Automatic Detection of Optical Signatures within and around Floating Tonga-Fiji Pumice Rafts Using MODIS,

VIIRS, and OLCI Satellite Sensors. Remote Sensing 13, 501. https://doi.org/10.3390/rs13030501

Zhang, H., Che, H., Xia, J., Cheng, Q., Qi, D., Cao, J., Luo, Y., 2022. Sedimentary CaCO3 Accumulation in the Deep West Pacific Ocean. Front. Earth Sci. 10, 857260. https://doi.org/10.3389/feart.2022.857260

Zhang, Q., Snow, J.T., Holdship, P., Price, D., Watson, P., Rickaby, R.E.M., 2018. Direct measurement of multi-elements in high matrix samples with a flow injection ICP-MS: application to the extended *Emiliania huxleyi* Redfield ratio. J. Anal. At. Spectrom. 33, 1196–1208. https://doi.org/10.1039/C8JA00031J

Zierenberg, R.A., Adams, M.W.W., Arp, A.J., 2000. Life in extreme environments: Hydrothermal vents. Proceedings of the National Academy of Sciences 97, 12961–12962. https://doi.org/10.1073/pnas.210395997

Geochimica and Cosmochimica Acta

Supporting Information for

Temporal and spatial variability in the hydrothermal signature of sinking particles and sediments in the Western Tropical South Pacific Ocean

Chloé Tilliette[1], Frédéric Gazeau[1], Valérie Chavagnac[2], Nathalie Leblond[1], Maryline Montanes[1], Karine Leblanc[3], Sabine Schmidt[4], Bruno Charrière[5], Nagib Bhairy[3], Cécile Guieu[1*]

[1]Sorbonne Université, CNRS, Laboratoire d'Océanographie de Villefranche, LOV, 06230, Villefranche-sur-Mer, France
[2]Géosciences Environnement Toulouse, GET, CNRS, UPS, Université de Toulouse, IRD, Toulouse, France
[3]Aix Marseille Univ., Université de Toulon, CNRS, IRD, MIO, Marseille, France.
[4]CNRS, UMR 5805 EPOC, Université de Bordeaux, Pessac, France
[5]Centre de Formation et de Recherche sur l'Environnement Méditerranéen (CEFREM, UMR CNRS 5110), Bât. U, Université de Perpignan, Via Domitia (UPVD), Perpignan, France

Contents of this file

Text S1. Physical conditions of the moored sediment traps

The average depth of the upper and lower sediment traps was 261 ± 16 m (n = 8141) and 1053 ± 15 m (n = 8104), respectively (*Fig. S1a, b*). Rare and short deepening events below 400 and 1190 m occurred in April and June. The average trap pitch angle at 200 m was -2 ± 1° and ranged from -10 to 3°. The trap pitch angle at 1000 m averaged -8 ± 4°, varying between -32 and 1°. It should be noted that high pitch angles (> 10 °) were rather rare, especially for the 200 m-trap (0.02% versus < 30% of the total period for the 1000 m-trap), and mainly associated with trap deepening events and current speeds exceeding 30 cm s^{-1}. The average current velocity at 200 and 1000 m was 10 ± 4 cm s^{-1} and 11 ± 5 cm s^{-1}, respectively. The west and east velocities were -1 ± 6 and 0 ± 7 cm s^{-1}, respectively, for the 200 m-trap. For the 1000 m-trap, they were 7 ± 5 and 1 ± 7 cm s^{-1} for the east and west directions, respectively. The maximum velocities reached were 25 and 36 cm s^{-1} for the 1000 m-trap in east and west directions, respectively. At 200 m, the maximum west and east velocities were reached at 32 and 38 cm s^{-1}, respectively.

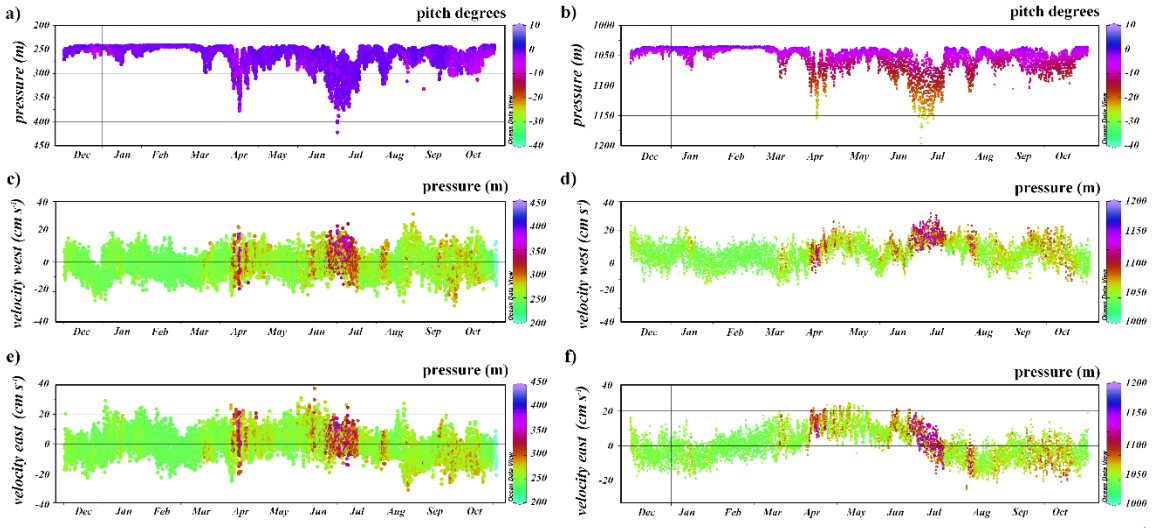

Figure S1. Plots showing inclination angles measured by inclinometers at 222 m **(a)** and 1030 m **(b)** and west and east velocities (cm s^{-1}) measured by current meters at 222 m **(c, e)** and 1030 m **(d, f)** during the fixed mooring line deployment period (from November 2019 to October 2020).

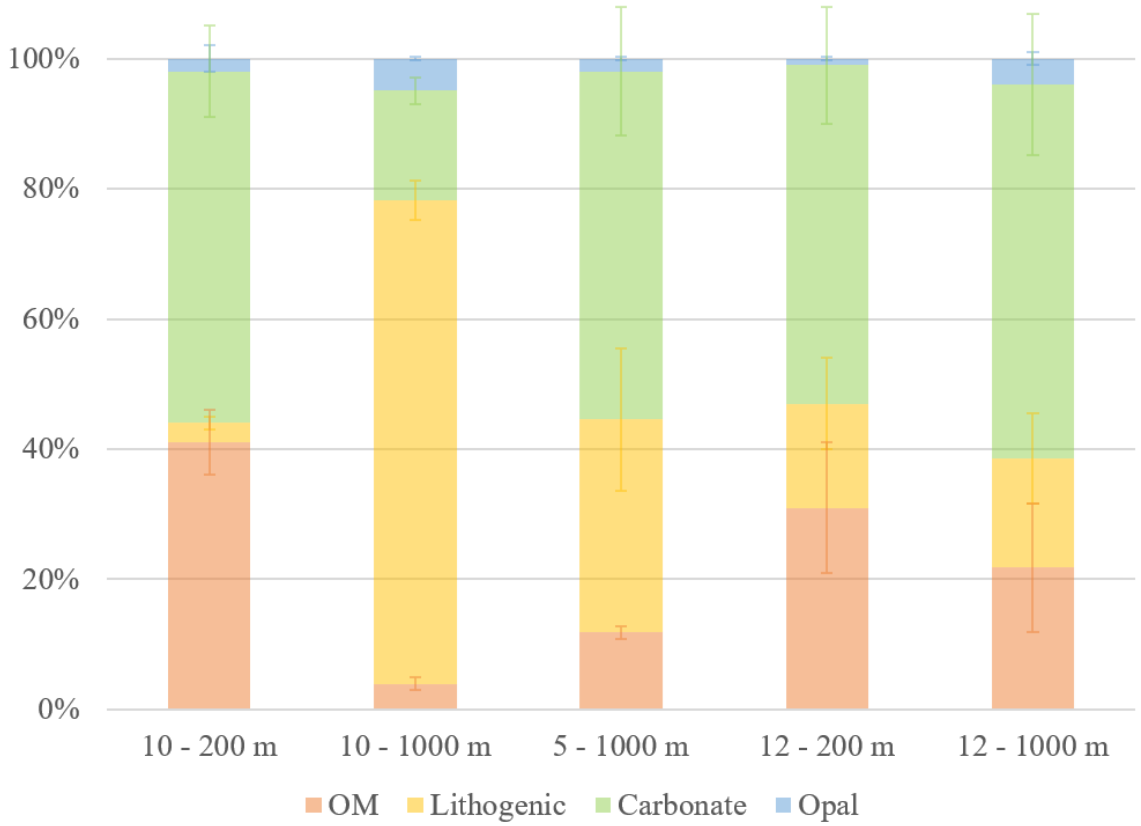

Figure S2. Cumulative histogram of the different fractions of material collected in the sediment traps, averaged over the entire deployment period. Orange: organic matter, blue: opal, green: calcium carbonate and yellow: lithogenic material.

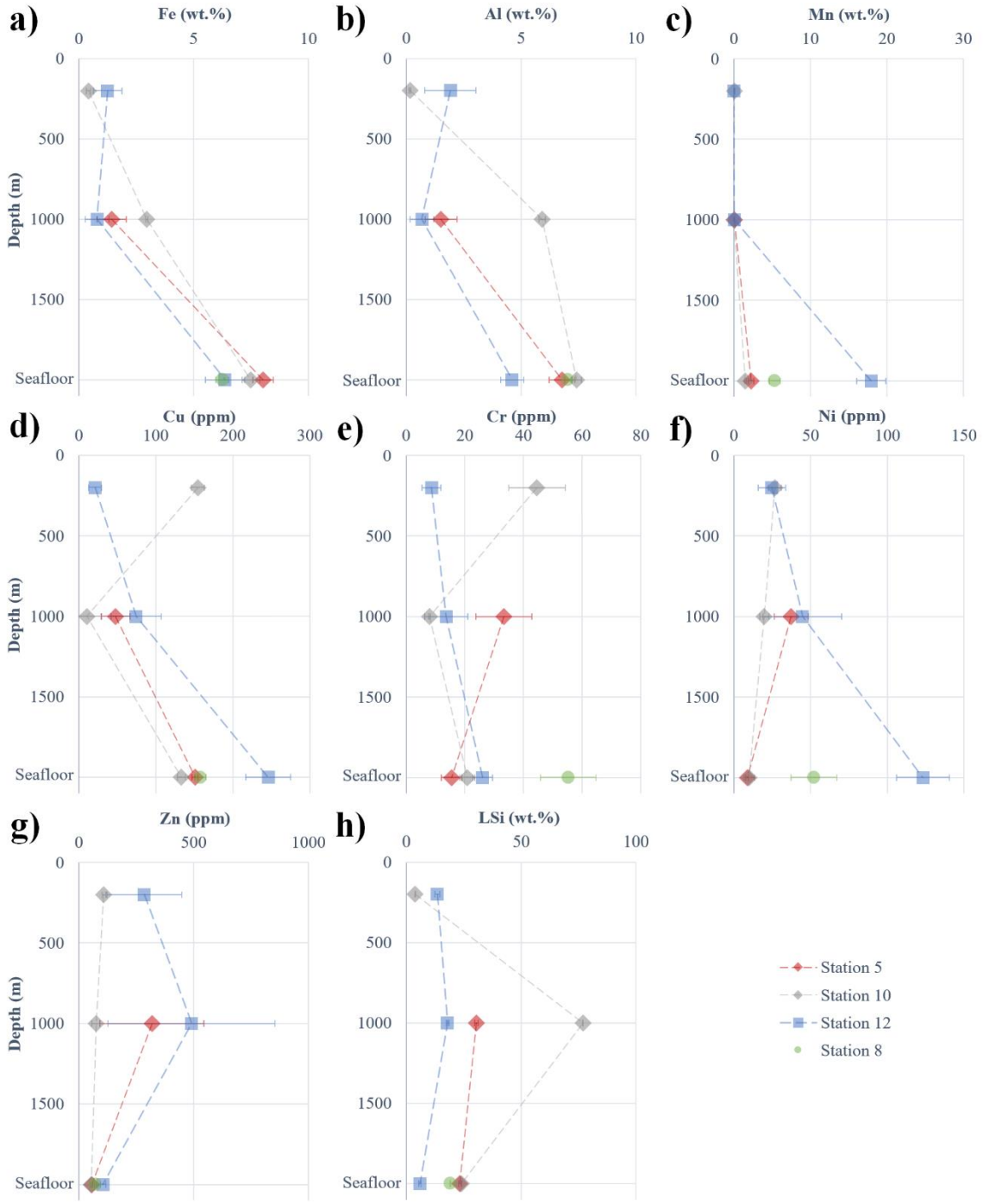

Figure S3. Profiles of particulate **(a)** iron (Fe), **(b)** aluminum (Al), **(c)** manganese (Mn), **(d)** copper (Cu), **(e)** chromium (Cr), **(f)** nickel (Ni), **(g)** zinc (Zn), and **(h)** lithogenic silica (LSi) for the different stations. Fe, Al, Mn and LSi are expressed in wt.% while Cu, Cr, Ni and Zn are expressed in ppm.

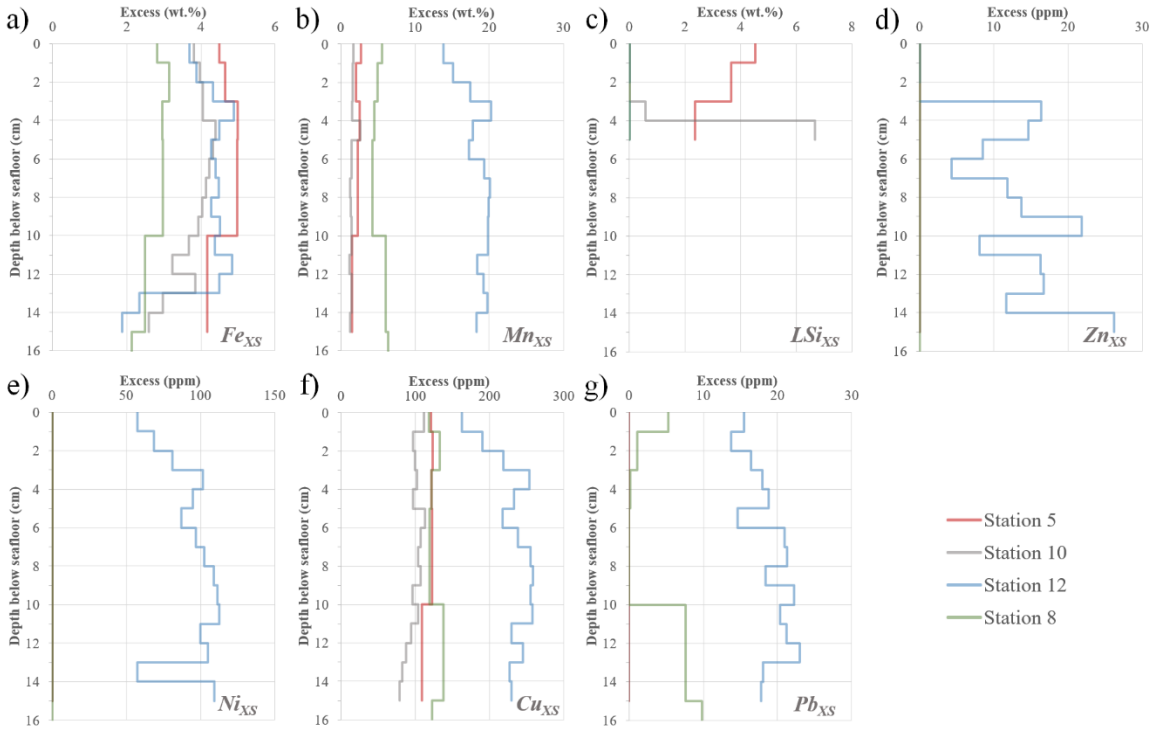

Figure S4. Profiles of particulate **(a)** iron (Fe), **(b)** aluminum (Al), **(c)** manganese (Mn), **(d)** calcium (Ca), **(e)** lithogenic silica (LSi), **(f)** zinc (Zn), **(g)** nickel (Ni), **(h)** copper (Cu), **(i)** lead (Pb) and **(j)** chromium (Cr) from the 15 cm of sediment cored during the cruise. Fe, Al, Mn, Ca and LSi are expressed in wt.% and Zn, Ni, Cu, Pb and Cr are expressed in ppm.

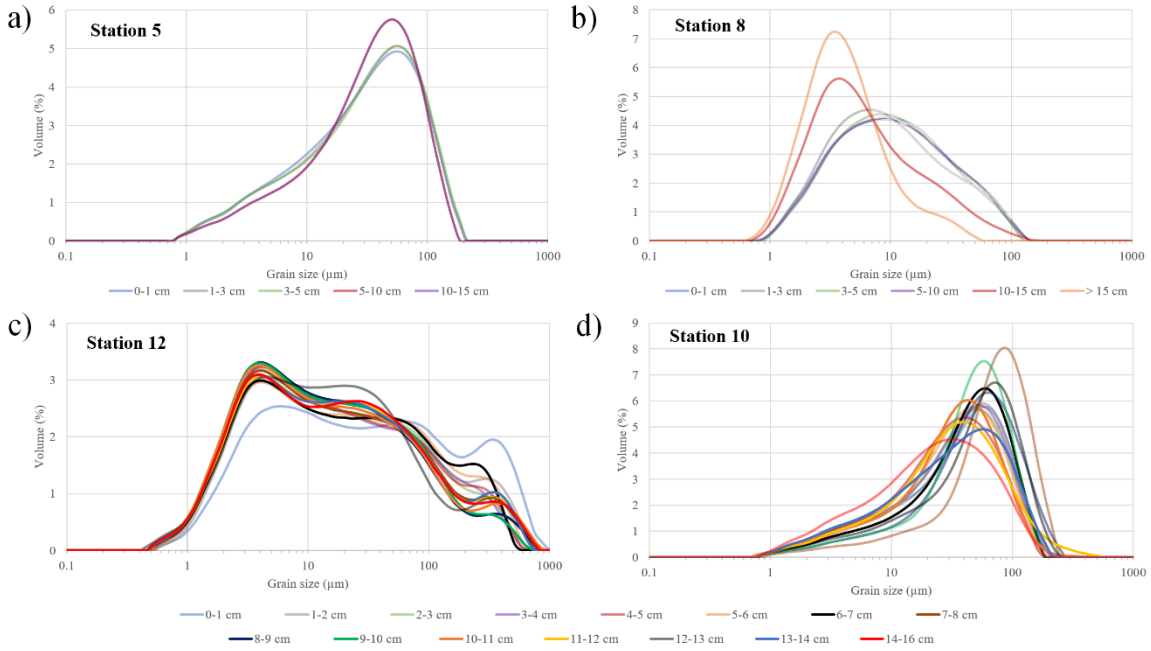

Figure S5. Grain size distribution in volume of seafloor sediments at stations **(a)** 5, **(b)** 8, **(c)** 12 and **(d)** 10. Each curve represents a slice of sediment.

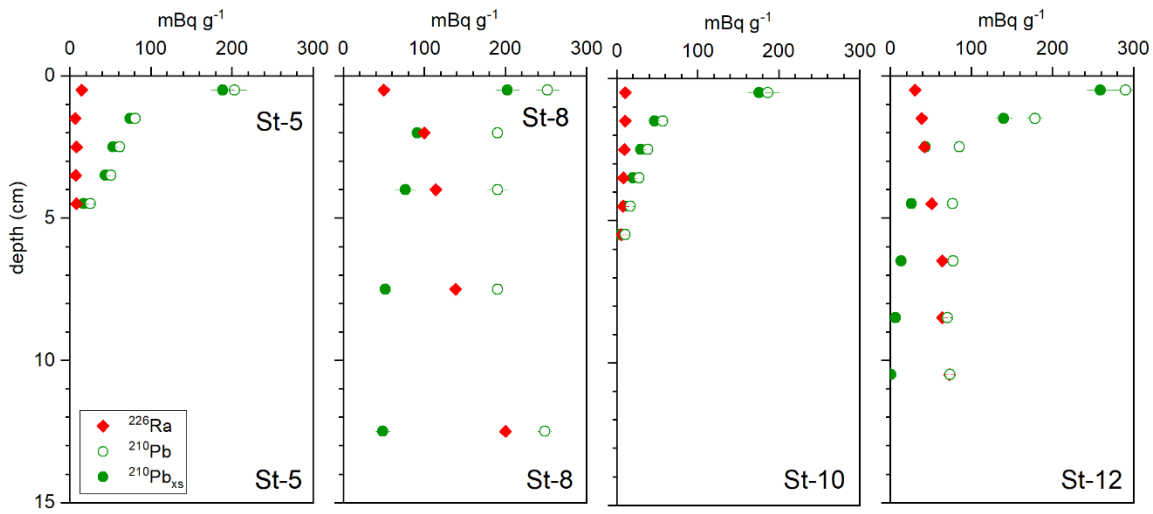

Figure S6. Depth profiles of ^{226}Ra, ^{210}Pb and $^{210}Pb_{XS}$ activities

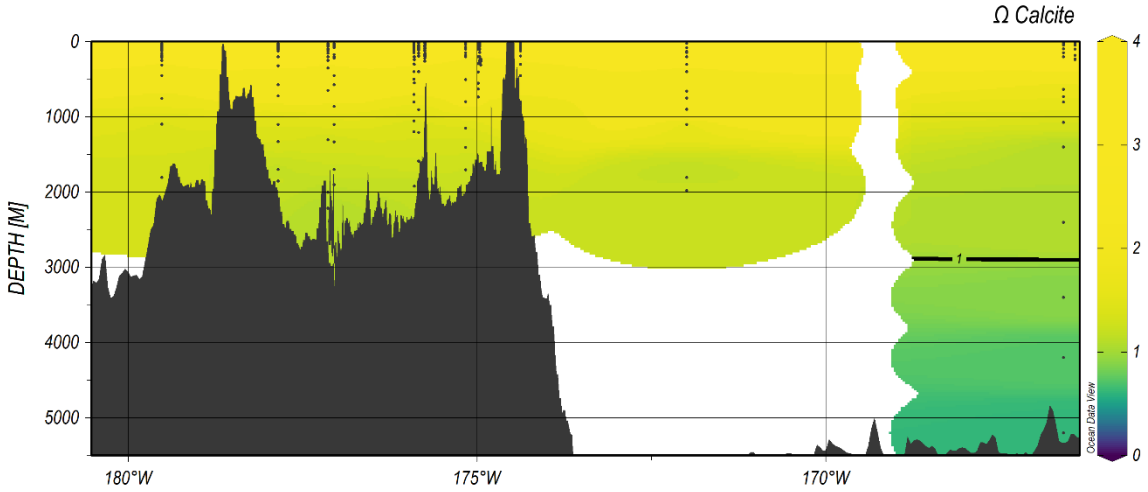

Figure S7. Calcite saturation rates on the cruise transect. Rates were calculated from pH and total alkalinity data via the *seacarb* package of R software (Lavigne and Gattuso, 2010). The calcite dissolution threshold, corresponding to the lysocline, is represented by a black line ($\Omega < 1$). The passage of this layer results in a marked increase in the dissolution rate of $CaCO_3$. It is located not far from the carbonate compensation depth, where the dissolution rate is equal to the formation rate.

Table S1. Percentage recovery of GBW certified reference material, blanks and limits of detection and quantification (in ppm) for each element analyzed by ICP-OES.

	Fe	Al	Ca	Mn	Cu	Zn	Cr	Pb	Ni
GBW percent recovery	104	101	100	102	113	103	111	80	105
Blanks	< DL	< DL	12 ± 1	15 ± 1	3.5 ± 1.9	1.6 ± 0.6	0.8 ± 0.6	2.6 ± 0.7	< DL
Detection limit	0.3	0.8	*n.d.*	0.2	1	0.5	0.7	*n.d.*	1.3
Quantification limit	0.6	2.7	*n.d.*	0.3	1.9	1.1	1.6	*n.d.*	3.5

Note. GBW is a marine reference sediment provided by the National Research Council for Certified Reference Materials (Canada). ICP-OES stands for Inductively-Coupled Plasma Optical Emission Spectrometry.

Table S2. Estimated calcium carbonate fraction in sinking material and seafloor sediment from %PIC or %Ca

Sample	Collecting day	Sampling period	$CaCO_3$ from PIC	$CaCO_3$ from Ca
		day	*%*	*%*
TD-ST5 1000-1	11/10/2019	1.0	40.1	43.0
TD-ST5 1000-2	11/11/2019	1.0	71.7	65.0
TD-ST5 1000-3	11/12/2019	1.0	73.6	66.0
TD-ST5 1000-4	11/13/2019	1.0	52.4	50.8
TD-ST5 1000-5	11/14/2019	1.0	44.8	43.1
TD-ST10 1000-1	11/24/2019	1.0	14.9	19.7
TD-ST10 1000-2	11/25/2019	1.0	9.6	14.2
TD-ST10 1000-3	11/26/2019	1.0	13.2	16.2
TD-ST10 1000-4	11/27/2019	1.0	14.3	18.6
TD-ST10 200-1	11/24/2019	1.0	n.d.	44.4
TD-ST10 200-2	11/25/2019	1.0	n.d.	55.6
TD-ST10 200-3	11/26/2019	1.0	n.d.	65.4
TD-ST10 200-4	11/27/2019	1.0	n.d.	49.2
TF-200-01	12/2/2019	14.0	61.4	49.1
TF-200-02	12/16/2019	14.0	52.5	47.6
TF-200-03	12/29/2019	14.0	63.6	57.1
TF-200-04	1/12/2020	14.0	46.0	50.1
TF-200-05	1/26/2020	14.0	23.3	40.3
TF-200-06	2/9/2020	14.0	4.6	47.7
TF-200-07	2/23/2020	14.0	69.5	49.5
TF-200-08	3/8/2020	14.0	81.8	35.8
TF-200-09	3/22/2020	14.0	44.5	54.7

TF-200-10	4/5/2020	14.0	28.8	48.2
TF-200-11	4/19/2020	14.0	41.0	68.1
TF-200-12	5/3/2020	14.0	38.4	60.3
TF-200-13	5/17/2020	14.0	53.8	63.6
TF-200-14	5/31/2020	14.0	52.3	66.3
TF-200-15	6/14/2020	14.0	35.8	63.9
TF-200-16	6/28/2020	14.0	63.7	100.4
TF-200-17	7/12/2020	14.0	40.7	81.4
TF-200-18	7/26/2020	14.0	62.7	53.2
TF-200-19	8/9/2020	14.0	49.9	60.4
TF-200-20	8/23/2020	14.0	52.6	56.1
TF-200-21	9/6/2020	14.0	23.9	66.9
TF-200-22	9/20/2020	14.0	61.5	67.2
TF-200-23	10/4/2020	14.0	25.4	50.3
TF-200-24	10/18/2020	14.0	17.6	60.3
TF-1000-01	12/2/2019	14.0	56.8	63.1
TF-1000-02	12/16/2019	14.0	59.4	56.3
TF-1000-03	12/29/2019	14.0	60.9	56.6
TF-1000-04	1/12/2020	14.0	69.3	62.4
TF-1000-05	1/26/2020	14.0	53.0	59.5
TF-1000-06	2/9/2020	14.0	54.8	61.1
TF-1000-07	2/23/2020	14.0	51.9	65.6
TF-1000-08	3/8/2020	14.0	60.1	58.5
TF-1000-09	3/22/2020	14.0	57.4	75.1
TF-1000-10	4/5/2020	14.0	64.1	68.2
TF-1000-11	4/19/2020	14.0	60.9	38.5
TF-1000-12	5/3/2020	14.0	65.3	67.2
TF-1000-13	5/17/2020	14.0	77.8	54.1
TF-1000-14	5/31/2020	14.0	12.0	26.0
TF-1000-15	6/14/2020	14.0	58.4	67.9
TF-1000-16	6/28/2020	14.0	59.6	143.4
TF-1000-17	7/12/2020	14.0	49.3	94.4
TF-1000-18	7/26/2020	14.0	61.9	59.2
TF-1000-19	8/9/2020	14.0	71.8	75.0
TF-1000-20	8/23/2020	14.0	14.1	47.2
TF-1000-21	9/6/2020	14.0	38.3	194.1
TF-1000-22	9/20/2020	14.0	72.4	139.3
TF-1000-23	10/4/2020	14.0	93.2	33.3
TF-1000-24	10/18/2020	14.0	69.1	85.0
SC-ST5 00-01 cm	-	-	2.1	13.3
SC-ST5 01-03 cm	-	-	0.9	12.7
SC-ST5 03-05 cm	-	-	1.0	15.2

SC-ST5 05-10 cm	-	-	1.0	15.5
SC-ST5 10-15 cm	-	-	3.9	18.7
	-	-	0.0	0.0
SC-ST10 00-01 cm	-	-	8.0	22.4
SC-ST10 01-02 cm	-	-	6.3	19.7
SC-ST10 02-03 cm	-	-	5.1	18.9
SC-ST10 03-04 cm	-	-	4.6	18.8
SC-ST10 04-05 cm	-	-	0.8	12.7
SC-ST10 05-06 cm	-	-	3.8	18.1
SC-ST10 06-07 cm	-	-	2.9	17.8
SC-ST10 07-08 cm	-	-	1.4	16.7
SC-ST10 08-09 cm	-	-	2.9	17.6
SC-ST10 09-10 cm	-	-	3.9	18.6
SC-ST10 10-11 cm	-	-	4.4	18.0
SC-ST10 11-12 cm	-	-	3.0	16.1
SC-ST10 12-13 cm	-	-	2.6	18.1
SC-ST10 13-14 cm	-	-	3.7	16.5
SC-ST10 14-16 cm	-	-	3.4	15.4
	-	-		
SC-ST12 00-01 cm	-	-	64.0	69.6
SC-ST12 01-02 cm	-	-	62.0	70.9
SC-ST12 02-03 cm	-	-	62.9	67.5
SC-ST12 03-04 cm	-	-	64.0	64.7
SC-ST12 04-05 cm	-	-	64.8	75.1
SC-ST12 05-06 cm	-	-	64.9	64.2
SC-ST12 06-07 cm	-	-	66.1	67.8
SC-ST12 07-08 cm	-	-	65.4	70.5
SC-ST12 08-09 cm	-	-	64.2	67.1
SC-ST12 09-10 cm	-	-	65.2	68.6
SC-ST12 10-11 cm	-	-	64.4	69.1
SC-ST12 11-12 cm	-	-	64.9	72.9
SC-ST12 12-13 cm	-	-	64.0	67.9
SC-ST12 13-14 cm	-	-	62.8	64.3
SC-ST12 14-15 cm	-	-	63.0	66.3
	-	-		
SC-ST8 00-01 cm	-	-	0.4	6.3
SC-ST8 01-03 cm	-	-	0.2	7.2
SC-ST8 03-05 cm	-	-	0.2	7.1
SC-ST8 05-10 cm	-	-	0.2	6.8
SC-ST8 10-15 cm	-	-	0.2	4.6
SC-ST8 >>15 cm	-	-	0.4	3.3

Note. The calcium carbonate fraction can be estimated from %PIC (%CaCO3 = %PIC × 8.33) or %Ca (%CaCO3 = 0.4 × %Ca). The calcium carbonate fraction of some samples was overestimated (> 100% of total collection weight) with the %Ca method. TD refers to drifting traps. TF refers to

fixed trap (Station 12 only). SC refers to sediment cores. PIC stands for particulate inorganic carbon.

Table S3. Highlights of the productivity measured at the stations studied during the TONGA cruise (austral summer conditions).

Sample	Station 5	Station 8	Station 10	Station 12
Primary productivity	90	< 35	145	n.d.
N_2 fixation	2727	225	1803	n.d.
Max total Chl-*a*	0.45	0.22	0.38	0.33
Cyanobacteria	70.3 ± 4.4	65.1 ± 7.5	68.6 ± 4.5	65.3 ± 4.6
Coccolithophores	22.9 ± 5.1	22.2 ± 3.6	24.8 ± 3.8	25.4 ± 4.0
Dinoflagellates, diatoms	6.7 ± 3.9	12.7 ± 7.9	6.5 ± 3.3	9.1 ± 4.3

Note. Primary production is in mmol C m^{-2} d^{-1}, dinitrogen (N_2) fixation is in µmol N m^{-2} d^{-1}. Maximum total chlorophyll-*a* (Chl-*a*) is in mg m^{-3}. The major groups contributing to total Chl-*a* are represented in %. Photosynthetic pigment data were obtained by high-performance liquid chromatography (Van Heukelem and Thomas, 2001). The contribution of cyanobacteria, coccolithophores, dinoflagellates and diatoms to total Chl-*a* was estimated from zeaxanthin, 19'-hexanoyloxyfucoxanthin, peridinin and fucoxanthin, respectively, following Uitz et al. (2006). The data presented in this table will be accessible as soon as they are published on the LEFE-CYBER database (http://www.obs-vlfr.fr/proof/php/TONGA/tonga.php).

Table S4. Boström index values in each cup of the traps and in each sediment slice.

Station	Date/slice	Depth	Fe_{cfb}	Al_{cfb}	Mn_{cfb}	Boström index
-	*-/cm*	*m*		*wt.%*		-
Station 5	11/10/2019	1000-01	0.97	1.01	0.03	50.31
	11/11/2019	1000-02	1.99	2.15	0.05	51.24
	11/12/2019	1000-03	2.44	2.60	0.07	50.87
	11/13/2019	1000-04	0.92	0.96	0.03	50.49
	11/14/2019	1000-05	0.80	0.83	0.03	50.01
	00-01 cm	Seafloor	7.52	6.11	2.78	37.22
	01-03 cm	Seafloor	7.65	6.05	2.09	38.33
	03-05 cm	Seafloor	8.66	7.38	2.58	39.64
	05-10 cm	Seafloor	8.48	7.05	2.35	39.44
	10-15 cm	Seafloor	7.81	7.34	1.54	43.96
Station 10	11/24/2019	200-01	0.47	0.22	0.08	28.61
	11/25/2019	200-02	0.55	0.09	0.10	11.64
	11/26/2019	200-03	0.37	0.17	0.12	26.28
	11/27/2019	200-04	0.28	0.15	0.09	28.66
	11/24/2019	1000-01	3.03	5.88	0.01	65.92
	11/25/2019	1000-02	2.99	6.17	0.01	67.35
	11/26/2019	1000-03	2.87	5.81	0.00	66.93
	11/27/2019	1000-04	2.93	5.79	0.01	66.34
	00-01 cm	Seafloor	7.48	7.38	1.78	44.37
	01-02 cm	Seafloor	7.69	7.50	1.65	44.54
	02-03 cm	Seafloor	7.84	7.63	1.69	44.47
	03-04 cm	Seafloor	7.67	7.30	1.58	44.11
	04-05 cm	Seafloor	7.51	6.28	1.46	41.19
	05-06 cm	Seafloor	8.07	7.53	1.54	43.95
	06-07 cm	Seafloor	8.02	7.67	1.49	44.64
	07-08 cm	Seafloor	7.90	7.58	1.36	45.01
	08-09 cm	Seafloor	7.83	7.65	1.43	45.21
	09-10 cm	Seafloor	7.66	7.52	1.49	45.10
	10-11 cm	Seafloor	7.41	7.53	1.46	45.90
	11-12 cm	Seafloor	6.80	7.18	1.23	47.20
	12-13 cm	Seafloor	7.71	7.80	1.49	45.87
	13-14 cm	Seafloor	6.59	7.30	1.50	47.42
	14-16 cm	Seafloor	6.27	7.40	1.29	49.46
Station 12	12/2/2019	200-01	0.13	0.12	0.006	47.00
	12/16/2019	200-02	0.04	0.02	0.003	34.90
	12/29/2019	200-03	0.73	1.03	0.003	58.39
	1/12/2020	200-04	0.99	1.70	0.003	63.18
	1/26/2020	200-05	0.53	1.02	0.002	65.76
	2/9/2020	200-06	0.69	0.97	0.002	58.25
	2/23/2020	200-07	0.75	0.66	0.003	46.83
	3/8/2020	200-08	2.07	2.44	0.006	54.10
	3/22/2020	200-09	1.73	2.94	0.007	62.86
	4/5/2020	200-10	1.35	2.77	0.006	67.13
	4/19/2020	200-11	1.02	2.42	0.007	70.07
	5/3/2020	200-12	0.89	1.83	0.006	67.15
	5/17/2020	200-13	1.83	3.38	0.008	64.74
	5/31/2020	200-14	2.46	3.10	0.011	55.63
	6/14/2020	200-15	3.64	7.33	0.008	66.80
	6/28/2020	200-16	1.84	0.32	0.003	14.73
	7/12/2020	200-17	1.04	1.50	0.004	58.95
	7/26/2020	200-18	0.20	0.06	0.001	21.44
	8/9/2020	200-19	1.34	2.39	0.003	64.01
	8/23/2020	200-20	0.92	1.21	0.003	56.78
	9/6/2020	200-21	1.68	2.36	0.007	58.26
	9/20/2020	200-22	1.80	2.15	0.004	54.43
	10/4/2020	200-23	1.45	3.09	0.002	68.09
	10/18/2020	200-24	0.91	1.17	0.005	55.89
	12/2/2019	1000-01	0.94	0.63	0.05	38.93
	12/16/2019	1000-02	2.88	3.08	0.10	50.74
	12/29/2019	1000-03	1.49	1.37	0.07	46.72

	1/12/2020	1000-04	1.44	1.64	0.03	52.68
	1/26/2020	1000-05	0.53	0.26	0.05	31.07
	2/9/2020	1000-06	0.75	0.54	0.06	39.96
	2/23/2020	1000-07	0.77	0.34	0.06	29.36
	3/8/2020	1000-08	1.27	1.11	0.09	44.93
	3/22/2020	1000-09	0.91	0.61	0.08	38.22
	4/5/2020	1000-10	0.71	0.46	0.06	37.42
	4/19/2020	1000-11	0.49	0.34	0.04	39.02
	5/3/2020	1000-12	0.28	0.15	0.03	32.88
	5/17/2020	1000-13	0.52	0.45	0.05	43.85
	5/31/2020	1000-14	0.05	0.05	0.01	48.61
	6/14/2020	1000-15	0.35	0.14	0.03	26.98
	6/28/2020	1000-16	0.25	0.25	0.02	48.04
	7/12/2020	1000-17	0.27	0.34	0.02	53.71
	7/26/2020	1000-18	0.33	0.31	0.03	46.07
	8/9/2020	1000-19	0.69	0.62	0.05	45.65
	8/23/2020	1000-20	0.04	0.04	0.00	50.44
	9/6/2020	1000-21	0.18	0.17	0.01	47.50
	9/20/2020	1000-22	0.50	0.45	0.04	45.70
	10/4/2020	1000-23	2.85	2.53	0.20	45.33
	10/18/2020	1000-24	0.63	0.46	0.04	40.57
	00-01 cm	Seafloor	5.75	4.17	13.83	17.56
	01-02 cm	Seafloor	6.09	4.47	15.16	17.37
	02-03 cm	Seafloor	6.77	4.92	17.49	16.87
	03-04 cm	Seafloor	7.71	5.70	20.26	16.92
	04-05 cm	Seafloor	6.82	4.67	17.82	15.92
	05-06 cm	Seafloor	6.66	4.83	17.30	16.77
	06-07 cm	Seafloor	6.88	5.00	19.38	16.00
	07-08 cm	Seafloor	6.98	5.05	20.13	15.69
	08-09 cm	Seafloor	6.83	5.13	20.00	16.05
	09-10 cm	Seafloor	6.96	4.92	19.87	15.49
	10-11 cm	Seafloor	6.76	4.80	19.88	15.26
	11-12 cm	Seafloor	7.14	4.65	18.40	15.39
	12-13 cm	Seafloor	6.88	4.81	19.27	15.54
	13-14 cm	Seafloor	3.51	2.35	9.75	13.41
	14-15 cm	Seafloor	3.66	3.61	18.33	14.10
Station 8	00-01 cm	Seafloor	6.12	6.63	5.59	36.16
	01-03 cm	Seafloor	6.69	7.15	4.99	37.98
	03-05 cm	Seafloor	6.45	7.05	4.55	39.06
	05-10 cm	Seafloor	6.44	6.99	4.34	39.35
	10-15 cm	Seafloor	6.13	7.33	6.15	37.37
	>>15 cm	Seafloor	5.64	7.08	6.45	36.93

Note. The concentrations in calcium-carbonate-free basis (*cfb*) of the elements used for the calculation of the index (Al_{cfb}, Fe_{cfb}, Mn_{cfb}) are also represented.